Imaging surface topography with coherent x-ray reflectivity: Theory, kinematics, and simulations

Irene Calvo-Almazán,[1,2] Anusheela Das,[3] Ana F. Suzana,[3] Fernando Bartolomé,[1,2] and Paul Fenter[3,*]

[1]*Departamento de Física de la Materia Condensada, Universidad de Zaragoza, Zaragoza 50009, Spain*

[2]*Instituto de Nanociencia y Materiales de Aragón, CSIC-Universidad de Zaragoza, Zaragoza 50009, Spain*

[3]*Chemical Sciences and Engineering Division, Argonne National Laboratory, Lemont, Illinois 60439, USA*

(Received 28 October 2025; revised 16 December 2025; accepted 24 December 2025; published 6 February 2026)

A theoretical formalism is described for understanding coherent x-ray reflectivity (CXR) from the surface of a semi-infinite crystal having a variable surface topography, described by the height profile $h(x, y)$. The surface topography is imaged as a complex "effective density," obtained from the phasing and inversion of the coherent x-ray reflectivity data, measured through a rocking scan centered at a vertical momentum transfer Q_z^0 and a vertical range ΔQ_z. The formalism predicts that the effective density has an amplitude with a maximum located at the surface height for each position within the surface plane. The phase of the effective density has a lateral variation that is controlled by the surface height and a vertical variation that reflects a combination of the interfacial structure and specific choice of measurement conditions. This understanding enables direct observation of nanometer-scale interfacial topography, i.e., $h(x, y)c_s$ (where c_s is the vertical substrate lattice parameter) with Å-scale sensitivity to surface height. Numerical simulations illustrate and confirm the theoretical results. These results show how the interpretation of the interfacial density phase obtained by CXR data inversion (i.e., surface topography with respect to a flat surface) is conceptually similar to that previously known for Bragg coherent diffraction imaging (BCDI) measurements of isolated nanoparticles (i.e., lattice displacements with respect to an ideal crystal lattice). This suggests that CXR can be thought of as a form of dark field imaging with respect to the bright field BCDI approach. An implication of these results is that interfacial imaging may bypass some of the significant challenges associated with BCDI imaging of multiple particles having different orientations.

DOI: 10.1103/q75z-gk3l

I. INTRODUCTION

Imaging crystalline surfaces and interfaces has been a long-standing challenge for coherent x-ray imaging due to their very low scattering cross section. However, this situation is rapidly improving with the advent of highly brilliant beams in the hard x-ray regime (with incident energies equal to or above 8 keV) produced at fourth generation synchrotrons. These radiation sources offer new possibilities for imaging weakly scattering systems thanks to an increase in coherent flux by two to three orders of magnitude [1–3]. In this context, hard coherent x-rays are particularly well suited for probing nonideal interfacial systems (e.g., rough and irregular surfaces [4]). The high penetration capability of hard coherent x-rays allows for *in situ* imaging within environments that mimic realistic conditions. Additionally, phase contrast encodes deviations from ideal crystallinity and provides high sensitivity to nanoscopic topographical features such as steps, terraces, pits, or crystalline distortions [5–7].

The increasing availability of highly coherent beams at hard x-ray energies, coupled to advances in computing capabilities, has fostered the development of a diverse range of "coherent diffraction imaging" (CDI) techniques. These techniques involve fine sampling (or oversampling) of the diffracted intensity from an object illuminated by a coherent x-ray beam around a specific point in reciprocal space, using a two-dimensional (2D) detector [8]. The data collected are then processed numerically with algorithms to retrieve a complex-valued image of the system [9–13]. For crystalline systems, CDI measurements can be performed in *Bragg geometry* [Bragg coherent diffraction imaging (BCDI)] meaning the diffracted intensity is sampled around a Bragg reflection [14]. This enables the imaging of the structure and morphology of isolated nanosized crystals in three dimensions (3D) or of extended systems (through Bragg ptychography [15]). These methods can be applied under a wide variety of environmental conditions, achieving nanometric resolution and high sensitivity to the presence of atomic defects [12,16–22].

The use of coherent x-ray scattering to study surface topography has been explored previously and tested in third generation synchrotrons. To compensate for the low coherent flux of their beams, surface studies with coherent x-rays have often focused mostly on grazing or small incident angles [23–25] or used the x-ray photon correlation spectroscopy (XPCS) mode [26,27]. Vartanyants *et al.* first described the coherent x-ray reflectivity (CXR) method, demonstrating that

*Contact author: fenter@anl.gov

by laterally oversampling the reflectivity signal in the low-angle (i.e., Fresnel) regime, the morphology of a surface could be reconstructed using a phase retrieval algorithm [23]. Later, Zhu *et al.* extended the CXR method by combining it with ptychography and wide angle scattering geometry where they successfully inverted coherent diffraction patterns using the surface reflectivity data from a platinum surface to create interfacial images [28]. It was assumed, however, that the observed phase differences were due solely to topography. Those results also revealed some artifacts, the most notable of which were significant differences in the interfacial amplitudes between different domains (i.e., terraces of different heights). This is surprising since it would be expected that the surface would have a single type of termination (except for changes in surface height due to topography). These artifacts may have resulted from using algorithms designed for forward scattering data where the diffraction patterns necessarily would be centrosymmetric due to Friedel's law [29]. However, the measured signals (i.e., detector images) in a specular reflection geometry are inherently asymmetric due to the tilt of the detector plane (i.e., the Ewald sphere) in the reflection geometry at finite momentum transfer, as well as due to the asymmetry of the crystal truncation rod (CTR) shape that is inherent to surface reflectivity [30]. Consequently, the asymmetry in the registered diffracted intensity on the detector plane would necessarily be interpreted as a complex density (i.e., with both an amplitude and a phase), but the meaning of the phase has not been evaluated. More recently, 3D interfacial structure imaging has been addressed by combining coherent x-ray holography and grazing incidence scattering [25]. Finally, the x-ray photon correlation spectroscopy (XPCS) mode, where a series of diffraction patterns are collected while the system is evolving, could measure the different timescales associated to step dynamics [26] or terrace growth [27,31]. These coherent approaches can be compared to interfacial imaging obtained with incoherent illumination using an objective lens, referred to as x-ray reflection interface microscopy (XRIM) [32,33]. Surfaces imaged in XRIM appear with a spatially variable reflected intensity that is controlled by the beam illumination and topography appears as localized modulations of the reflected intensity at the step location. This step contrast is controlled by the phase change across the step (due to the combined effect of the step height and the scattering condition Q_z^0).

Here, we develop a theoretical formalism for CXR that reveals an expression for the complex-valued interfacial density obtained from the inverse Fourier transform of phased data, thereby revealing the information that can be derived from CXR measurements. We consider a specific measurement approach and geometry that follows the general outlines of BCDI, in which the measurement probes a 3D volume of reflected intensities through a "rocking scan" that selects a finite section of the specular crystal truncation rod (CTR), measured at a vertical momentum transfer Q_z^0 with a finite vertical range ΔQ_z, while measuring the diffuse scattering parallel to the interfacial plane. CXR results measured in this geometry have not been reported to our knowledge. We assume that the phases of the measured signals can be recovered using traditional phase retrieval algorithms that have been developed for CDI (including BCDI) [9–11].

Although we are following the well-defined approach of BCDI, it is useful to note that there are both similarities and differences in the use of CXR with respect to BCDI. Our previous work showed, using numerical simulations, that interfaces could be imaged using the magnitude of the interfacial densities obtained by inverse Fourier transform of the phased CXR data [34]. That work highlighted two fundamental differences between the diffracted intensities recorded in CXR and BCDI (i.e., a section of a CTR vs a Bragg peak, respectively). One of these differences lies in the inherent asymmetry of the intensity along the CTR at Q_z^0 away from the Bragg peak position $\boldsymbol{Q}_B$, which varies as $\sim 1/(Q_z - \boldsymbol{Q}_B)^2$ [30]. In the context of BCDI (in which the data are centered on the Bragg peak position), it is well known that the scattering intensities for an ideal nanocrystal are nominally symmetric with respect to $\boldsymbol{Q}_B$ and that observation of asymmetric intensities leads to a complex-valued density whose phase is proportional to projection of lattice displacements (i.e., strain) along the direction defined by $\boldsymbol{Q}_B$ [4]. The same consideration suggests that any density obtained using the inherently asymmetric CXR intensities (centered at Q_z^0 but not including the substrate Bragg peak) should be necessarily complex valued, but an understanding and interpretation of those phases has not been identified yet. A second difference is the need to explicitly account for the truncation of the CTR intensity that is imposed by any finite reciprocal space volume (i.e., the vertical region of interest, ROI).

The formalism that we report here shows that the interface appears as an isolated complex object that we refer to as an "effective density" ρ_{eff}. This object has the properties that (1) is discrete along the surface normal direction, where its width is resolution limited and controlled by the vertical resolution, and the vertical height, in z, at the interfacial density maximum follows the surface topography $h(x,y)$ (as shown previously by numerical simulations [34]); (2) is complex valued with a phase prefactor that depends solely on the interfacial height and also having a vertical phase gradient that is controlled by the intrinsic interfacial structure and measurement conditions; and (3) has an amplitude within the surface plane that is controlled by the beam illumination but which is also modulated by topography. We also discuss the constraints associated with the finite spatial resolution and the modulo-2π uncertainties in the height determined from the phase and define the conditions for which the topography can be recovered uniquely. Notably, the phase of the recovered effective density provides sensitivity to atomic-scale changes in surface heights that are substantially smaller than the experimental resolution (i.e., a form of "super-resolution" imaging). In addition, we explicitly account for important experimental details such as the nonorthogonal reciprocal space volume which is inherent to measurements using specular CXR measurements. Together, these insights enable the determination of the topography from the phase of the complex interfacial densities achieving sub-nm vertical sensitivity and a lateral resolution that is controlled by the data range (~10's of nm's) for experimentally accessible conditions.

The paper is organized as follows. First, we describe the scattering from an interface and derive a forward model for calculating the complex structure factor (i.e., the diffracted

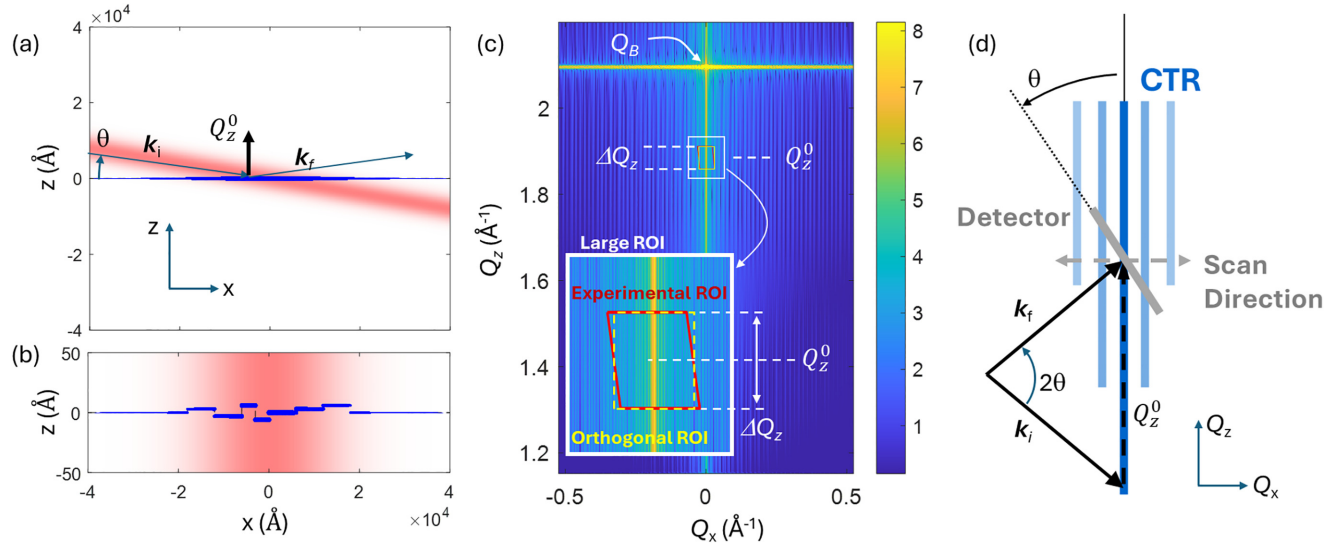

FIG. 1. Kinematics of coherent x-ray reflectivity (CXR). (a) Scattering geometry in real space where a finite-size coherent x-ray beam illuminates a crystalline surface at a fixed angle θ with respect to the surface, with coordinates x and z in the scattering plane. The momentum transfer $\boldsymbol{Q}_0 = \boldsymbol{k}_f - \boldsymbol{k}_i$ is the vector difference between the incoming and the outgoing $\boldsymbol{k}_f$ wave vectors and defines the scattering condition. (b) Detail of the surface topography (blue dots) and beam illumination (red region). Note that the apparent difference in beam direction is due to the limited vertical range with respect to (a). (c) The reciprocal space intensity distribution associated with the topography in (a) and (b), shown as $\log_{10}[\mathrm{I}(Q_x, Q_z)]$, and as a function of lateral and vertical momentum transfer (Q_x and Q_z, respectively), including the substrate Bragg peak at Q_B, the region of interest centered at $\boldsymbol{Q}_z^o$. A detail of the ROI is shown, inset, with both the oblique experimental ROI of a measurement (red box) and the "orthogonal ROI" that is used for comparison (in yellow), where a large ROI (white lines) is used to avoid artifacts in the calculation. The CTR is decorated with elongated speckles which contain structural information associated with the topographical features in the illuminated volume. (d) Schematic of the reciprocal space geometry showing the intensity (blue lines) from coherent illumination, the detector plane (gray line) on the Ewald sphere centered at $Q_z = \boldsymbol{Q}_z^o$ that is tilted by an angle equal to the incident angle, and the scan direction for a rocking scan along Q_x. This results in a tilted reciprocal space ROI [red box, (c)]. The detector extends along the Q_y direction which is perpendicular to the figure plane.

wavefield) for arbitrary interface topographies using the kinematic scattering theory. Then, we use this forward model to define the inverse problem where we derive the expected functional form for the effective interfacial density that would be obtained from the inversion of CXR data upon successful phase retrieval. We then explain how the specific constraints of experimental CXR measurements (i.e., the finite size and nonorthogonal shape of the sampled reciprocal space due to the tilt of the Ewald sphere) alter the imaged density and describe how intrinsic interfacial densities can be recovered. Finally, we outline the limits of this analysis and relevant extensions.

II. KINEMATIC THEORY FORMALISM: FORWARD AND INVERSE PROBLEMS

A. Total structure factor $F(\boldsymbol{Q})$

We consider the case where a finite-sized coherent x-ray beam having a field magnitude of $A_{3\mathrm{D}}(x, y, z)$, with energy E and wavelength $\lambda = hc/E$, is incident upon a semi-infinite crystalline solid having an electron density $\rho(x, y, z)$, at an angle θ, with respect to the surface plane (Fig. 1). Here, (x, y) are the basis vectors within the surface plane and z is the direction perpendicular to the surface plane [see Fig. 1(a)]. In that coordinate system the beam position in the surface plane is (x_0, y_0). Hence, (Q_x, Q_y) is the momentum transfer within the surface plane while Q_z is the component along the surface normal direction [see Fig. 1(b)]. The distribution of diffracted intensities is described by kinematic diffraction theory through a complex field called the *structure factor* $F(\boldsymbol{Q})$ [29,35]. Here the momentum transfer $\boldsymbol{Q} \equiv \boldsymbol{k_f} - \boldsymbol{k_i} = (Q_x, Q_y, Q_z)$ defines the scattering geometry (where $\boldsymbol{k_i}$ and $\boldsymbol{k_f}$ are, respectively, the incident and reflected wave vectors, and $|\boldsymbol{k_i}| = |\boldsymbol{k_f}| = 2\pi/\lambda$). The scattered intensity is calculated directly as $I \propto |F(\boldsymbol{Q})|^2$ for a fully coherent beam without ensemble average [23]. We do not consider the absolute scattering intensities for these calculations, and consequently the beam illumination is assumed to have a constant lateral size σ_t, with a Gaussian beam shape with unit magnitude $A_{3\mathrm{D}}(x, y, z) = \exp(-\frac{1}{2}\{(y - y_0)^2 + [x - x_0 + z/\tan(\theta)]^2\}/\sigma_t^2)$. This expression does not include the phase structure associated with a highly focused beam [36]. Therefore, this specific formalism is appropriate for experiments using long focal length beams, where the detector distance is comparable to the beam focal length, and with a modest beam size at the focus ($\sim$1 μm). More generally, the actual shape and phase structure of a focused beam can be included in the illumination function, and the additivity of the observed phase will combine contributions from the object and the beam.

The structure factor $F(\boldsymbol{Q})$ is determined from the electron density and the beam illumination within the assumption of kinematic diffraction theory which is appropriate for interfacial x-ray scattering [29]. The structure factor therefore is

calculated as the 3D Fourier transformation ($\mathcal{FT}$) of the illuminated volume [23]:

$$F(Q_x, Q_y, Q_z) \equiv \int_{\boldsymbol{x}} \int_{z} \mathrm{A_{3D}}(x, y, z)\rho(x, y, z) \times \exp[\mathrm{i}(Q_x x + Q_y y + Q_z z)]\mathrm{d}x\,\mathrm{d}y\,\mathrm{d}z = \mathcal{FT}[\mathrm{A_{3D}}\rho]. \quad (1)$$

Equation (1) constitutes a *forward model* transforming the structural features illuminated by the beam into a structure factor and its associated scattering intensities in reciprocal space [Fig. 1(c)]. This expression does not explicitly account for the attenuation of the x-ray beam into the substrate, which will be included explicitly in the derivation below.

When the phases are known, the unknown structure can be imaged using the complement to Eq. (1), by means of a 3D inverse Fourier transformation ($\mathcal{FT}^{-1}$). However, the finite volume of reciprocal space that is measured needs to be explicitly accounted for in the analysis. This is described by a window function $\hat{W}_{3D}(\boldsymbol{Q})$ that is centered at $\boldsymbol{Q} = [0, 0, Q_z^0]$ and having a vertical range of ΔQ_z [Fig. 1(c)]. The result is calculated as

$$\rho_{\mathrm{eff}}(\boldsymbol{x}) \equiv \exp\left[\mathrm{i}\, Q_z^0 z\right]\mathcal{FT}^{-1}[\mathbf{F}\ \hat{\mathbf{W}}_{\mathbf{3D}}] = \boldsymbol{FFT^{-1}}[\mathbf{F}\ \hat{\mathbf{W}}_{\mathbf{3D}}] = \exp\left[\mathrm{i}\, Q_z^0 z\right]\int \mathrm{F}(\boldsymbol{Q})\hat{W}_{3D}(\boldsymbol{Q})\exp\left[-\mathrm{i}(\boldsymbol{Q}\cdot\boldsymbol{x})\right]\mathrm{d}\boldsymbol{Q}. \quad (2)$$

Equation (2) defines the *inverse model* of Eq. (1), which transforms the information encoded in the structure factor into a complex-valued *effective density* ρ_{eff} (which is distinct from the sample density because many of its properties are affected directly by the specific details of the resolution function, as will be shown below). The prefactor $\exp[\mathrm{i}\, Q_z^0 z]$ accounts for the phase of the Fourier transform of data centered at Q_z^0 so that the effective density in Eq. (2) is equivalent to that obtained using an inverse fast Fourier transformation (FFT^{-1}), as is normally done in the analysis of BCDI data [35].

To ensure interfacial specificity, we focus on the condition where the probed reciprocal space volume includes a finite section of the crystal truncation rod (CTR) along Q_z and its associated diffuse scattering (as a function of Q_x and Q_y), while excluding any substrate Bragg peaks. As described previously through numerical calculations, the amplitude of the effective density is controlled by the product of the substrate electron density, the beam illumination, and the choice of the reciprocal space window [34]. The effective density is complex valued and, as we show below, its phase derives from two sources: the vertical asymmetry of the CTR (along Q_z) within the measured window function $\hat{W}_{3D}$, and the surface topography.

Equations (1) and (2) are similar in that they are both Fourier transforms (FT) of products of functions: the illuminated volume $A_{3D}\rho$ and the measured structure factors $F\ \hat{W}_{3D}$. Applying the Fourier convolution theorem [29,37], these expressions can be written as 3D convolutions ($\otimes$) of FTs:

$$F\left(Q_x, Q_y, Q_z\right) = \mathcal{FT}[\mathrm{A_{3D}}] \otimes \mathcal{FT}[\rho]; \quad (3.1)$$

$$\rho_{\mathrm{eff}}(\boldsymbol{x}) = \exp\left[\mathrm{i}\, \mathrm{Q}_z^0 z\right]\left\{\mathcal{FT}^{-1}[F] \otimes \mathcal{FT}^{-1}[\hat{W}_{3D}]\right\} = \exp\left[\mathrm{i}\, \mathrm{Q}_z^0 z\right][\mathrm{A}_{3D}\,\rho] \otimes \mathcal{FT}^{-1}[\hat{W}_{3D}]. \quad (3.2)$$

Thereby, Eqs. (3.1) and (3.2) describe the impact of the real-space illumination (i.e., beam size) on the distribution of diffracted intensities, and the role of the measured reciprocal space volume on the observed effective density, respectively. As shown in our previous work [34], the lateral width of the beam illumination A_{3D} in the surface plane induces a lateral broadening of the reciprocal space speckles (including the CTR, the Bragg peaks, and diffuse scattering) due to the finite beam size. Similarly, the finite vertical range of the measured reciprocal space volume $\hat{W}_{3D}$ ensures that ρ_{eff} is finite in extent in the vertical direction (unlike the semi-infinite electron density ρ) having a vertical width that is resolution limited. The lateral size of $\hat{W}_{3D}$ defines the spatial resolution of ρ_{eff} within the surface plane. In the next section, we examine the details of the *interfacial structure factor,* defined as $F_0 \equiv \mathcal{FT}[\rho]$. Then, we will derive an expression for the *effective density*, defined in Eqs. (2) and (3.2).

B. Interfacial structure factor $F_0(\boldsymbol{Q})$

The interfacial structure factor is defined as the 3D Fourier transform (FT) of the electron density for a surface with variable topography but uniform illumination (e.g., a plane wave):

$$F_0(\boldsymbol{Q}) \equiv \int \rho(\boldsymbol{x})\exp\left[\mathrm{i}\boldsymbol{Q}\cdot\boldsymbol{x}\right]\mathrm{d}^3\boldsymbol{x} = \mathcal{FT}[\rho]. \quad (4.1)$$

Since the electron density can be described as the sum of the atomic contributions at each lattice position i: $\rho(\boldsymbol{x}) = \sum_i \rho_i(\boldsymbol{x})$, the interfacial structure factor will be the direct sum of the corresponding Fourier transforms: $F_0(\boldsymbol{Q}) \propto \sum_i \mathcal{FT}[\rho_i(\boldsymbol{x})]$ [23]. This sum can be separated into a semi-infinite column of unit cells reproduced at each lateral lattice position (x_i, y_i) with a height corresponding to the surface height profile $h(x_i, y_i)$ at that position [Fig. 1(b)]. Therefore, the structure factor can be factorized into a term depending on the crystalline semi-infinite column $F_{\mathrm{col}}(\boldsymbol{Q})$ and another term that describes the interfacial topography $F_{\mathrm{top}}(\boldsymbol{Q})$, that is defined by $h(x_i, y_i)$ at each unit-cell position within the surface plane:

$$F_0(\boldsymbol{Q}) = F_{\mathrm{col}}(\boldsymbol{Q})F_{\mathrm{top}}(\boldsymbol{Q}). \quad (4.2)$$

This expression is general for any crystalline surface provided that the interfacial structure is identical at each surface unit cell [34]. In Eq. (4.2), all information concerning the vertical interfacial structure (i.e., subsurface structural displacements, surface reconstructions, as well as the presence of adsorbates and conformal thin films [38]) and the substrate lattice structure (i.e., atomic unit-cell structure, stacking of layers in orthogonal vs nonorthogonal lattices) is contained in the column structure factor $F_{\mathrm{col}}(Q_z)$ [30]. To simplify the derivation, we assume an orthogonal lattice with a surface that is ideally terminated (i.e., where each layer is identical) with a top layer at $z_0 = 0$, and a vertical lattice spacing c_s. In that case, the semi-infinite column of unit cells produces a

column structure factor which can be expressed as the product of a unit-cell form factor, describing the atomic arrangements within each unit cell and a CTR structure factor $F_{\mathrm{col}}(\boldsymbol{Q}) = F_{\mathrm{UC}}(\boldsymbol{Q})F_{\mathrm{CTR}}(Q_z)$ [30], where the CTR form factor is

$$F_{\mathrm{CTR}}(Q_z) \equiv \frac{1}{1-\beta\exp\left(-iQ_z c_s\right)}. \tag{4.3}$$

Here, c_s is the vertical lattice spacing, $\beta = \exp\{-c_s/[\Lambda\sin(\theta)]\}$ corresponds to the attenuation of the x-ray beam as it passes through one crystalline layer at an incident angle θ, and Λ is the x-ray attenuation length. Typical x-ray attenuation lengths are large with respect to atomic dimensions (e.g., $\Lambda = 90\,\mu\mathrm{m}$ for a 10-keV photon in calcium carbonate $CaCO_3$, corresponding to $\beta = 0.9999$ for an incident angle of $\theta = 11^\circ$). Thus, this term is typically ignored. Nevertheless, it plays an important part in the convergence of expressions derived below. The surface topography is assumed to be due to crystallographic roughness, where the surface height is $h(x, y)c_s$. The topographic structure factor then becomes [23]

$$\begin{aligned} F_{\mathrm{top}}(Q) &\equiv \sum_{x,y} \exp\left[iQ_z h(x,\ y)c_s\right]\exp[i(Q_x x + Q_y y)] \\ &= D\mathcal{FT}_{\mathbf{x}}\{\exp\left[iQ_z h(x,\ y)c_s\right]\}, \end{aligned} \tag{4.4}$$

where $\mathcal{DFT}_{\mathbf{x}}$ is the discrete Fourier transform within the surface plane.

C. Effective interfacial density $\rho_{\mathrm{eff}}(\boldsymbol{x})$

An expression for the effective interfacial density can be derived by combining Eq. (2) with the expression for the structure factor F [Eq. (3.1)] and using the definition of the *intrinsic structure* factor F_0 [Eq. (4.1)]:

$$\rho_{\mathrm{eff}}(\boldsymbol{x}) = \exp\left[\mathrm{i}Q_z^0 z\right]\mathcal{FT}^{-1}[\{\mathcal{FT}[\mathrm{A_{3D}}] \otimes F_0(\boldsymbol{Q})\}\hat{W}_{3\mathrm{D}}(\boldsymbol{Q})]. \tag{5}$$

Further simplification can be achieved by taking the special case where the illumination is perpendicular to the surface plane, so that its FT is separable into terms depending on the in-plane and vertical momentum transfers: $\mathcal{FT}[\mathrm{A_{3D}}(\boldsymbol{x})] = \hat{A}_{2\mathrm{D}}(Q_x, Q_y)\delta(Q_z)$. Note that this assumption eliminates a skewing of the reciprocal space ROI due to the tilt of the beam, as described previously [34], and simplifies the derivation, but does not alter the properties of ρ_{eff}, as will be shown below. Introducing the factorized form of the intrinsic structure factor [Eq. (5)] and applying the Fourier convolution theorem, the separability of Fourier transformations of the convolution product $\otimes = \otimes_x\otimes_y\otimes_z$ and of the 3D reciprocal space window $\hat{W}_{3\mathrm{D}}(\boldsymbol{Q}) = \hat{W}_{2\mathrm{D}}(Q_x, Q_y)\hat{W}_{1\mathrm{D}}(Q_z)$ yields the following result:

$$\begin{aligned} \rho_{\mathrm{eff}}(\boldsymbol{x}) = \exp\left[\mathrm{i}\,Q_z^0 z\right]\big\{&\mathrm{A_{2D}}(x, y)\delta[z - h(x, y)c_s]\otimes_z \rho_{\text{eff-0}}(z) \\ &\otimes_z \mathcal{FT}_z^{-1}[F_{\mathrm{UC}}(Q_z)]\big\}\otimes_{x,y}\mathrm{W_{2D}}(x, y). \end{aligned} \tag{6.1}$$

This expression shows that $\rho_{\mathrm{eff}}(\boldsymbol{x})$ can be described as convolutions along z and within the surface plane (x, y) of various terms: The first term $A_{2\mathrm{D}}(x, y)$ corresponds to the beam illumination within the surface plane. The term $\delta[z - h(x, y)c_s] = \mathcal{FT}^{-1}[\mathcal{FT}_x\{\exp\left[iQ_z h(x, y)c_s\right]\}]$ derives from the inverse FT (IFT) of the topographical structure factor defined in Eq. (4.4), and therefore can be understood as a representation of the *topography*. The term $W_{2\mathrm{D}}(x, y)$ is the lateral resolution function, arising from the IFT of the finite window in reciprocal space $\hat{W}_{2\mathrm{D}}(Q_x, Q_y)$. We have also defined an *intrinsic effective density*, $\rho_{\text{eff-0}}(z)$ as the IFT of the CTR structure factor in the Q_z direction over the range defined by the vertical window function:

$$\rho_{\text{eff-0}}(z) \equiv \mathcal{FT}_z^{-1}[F_{\mathrm{CTR}}(Q_z)\hat{W}_{1\mathrm{D}}(Q_z)]. \tag{6.2}$$

From the convolution of the delta function describing the topography with the intrinsic interfacial density, we then obtain the expression

$$\begin{aligned} \rho_{\mathrm{eff}}(\boldsymbol{x}) \equiv \exp\left[\mathrm{i}\,Q_z^0 z\right]\big\{&[\mathrm{A_{2D}}(x, y)\rho_{\text{eff-0}}[z - h(x, y)c_s]] \\ &\otimes_z \mathcal{FT}_z^{-1}[F_{\mathrm{UC}}(Q_z)]\big\}\otimes_{\boldsymbol{x}} W_{2\mathrm{D}}(\boldsymbol{x}). \end{aligned} \tag{6.3}$$

This shows the intuitive result that the lateral variation of the effective interfacial density is controlled by the beam illumination, and that the height of the interfacial density magnitude at any given position within the surface plane (x, y) is shifted along the surface normal direction as described by the surface topography $h(x, y)$, with a lateral "blurring" due to the convolution with the lateral window function $W_{2\mathrm{D}}(\boldsymbol{x})$ describing the real-space resolution.

D. Intrinsic effective density $\rho_{\text{eff-0}}(z)$

The *intrinsic effective density* $\rho_{\text{eff-0}}(z)$ is defined in Eq. (6.2) as the IFT of the CTR structure factor within the 1D window function $\hat{W}_{1\mathrm{D}}(Q_z, Q_z^0, \Delta Q_z)$, that is centered at Q_z^0 and has a vertical width ΔQ_z. Here, we derive a mathematical form for $\rho_{\text{eff-0}}$, which reveals the specific characteristics of an interface located at $h(x, y) = 0$. This can also be written as a convolution of IFTs, using the Fourier convolution theorem: $\rho_{\text{eff-0}}(z) = \mathcal{FT}_z^{-1}[F_{\mathrm{CTR}}(Q_z)] \otimes \mathcal{FT}_z^{-1}[\hat{W}_{1\mathrm{D}}(Q_z)]$. In the next paragraphs, we will look at each term individually.

The IFT of $F_{\mathrm{CTR}}(Q_z)$ can be explicitly calculated, using the expansion of a geometric series of the form $\frac{1}{1-r} = \sum_{n=0}^{\infty} r^n$ where $r \equiv \beta\exp(-iQ_z c_s)$:

$$\begin{aligned} \mathcal{FT}_z^{-1}\{F_{\mathrm{CTR}}(Q_z)\} &= \mathcal{FT}_z^{-1}\left\{\frac{1}{1-\beta\exp(-iQ_z c_s)}\right\} \\ &= \mathcal{FT}_z^{-1}\left\{\sum_{n=0}^{\infty}\beta^n\exp(-inQ_z c_s)\right\} \\ &= \sum_{n=0}^{\infty}\beta^n\delta(z + nc_s). \end{aligned} \tag{7.1}$$

This yields a semi-infinite summation of Dirac delta functions corresponding to the semi-infinite series of atomic layers, i.e., at $z = -nc_s$ (where $n = 0, 1, 2, \ldots$). The IFT of the 1D window can be calculated as

$$\begin{aligned} \mathcal{FT}_z^{-1}\{W_{1\mathrm{D}}(\mathrm{Q}_z)\} &= \int_{-\frac{\Delta Q_z}{2}}^{\frac{\Delta Q_z}{2}} \exp\left[-\mathrm{i}\left(q_z + Q_z^0\right)z\right]\mathrm{d}q_z \\ &= \exp\left[-\mathrm{i}Q_z^0 z\right]\Delta Q_z\,\mathrm{sinc}\left(\frac{\Delta Q_z}{2}z\right), \end{aligned} \tag{7.2}$$

where $\mathrm{sinc}(x) \equiv \sin(x)/x$ and $q_z \equiv Q_z - Q_z^0$ is the reduced momentum transfer describing the reciprocal space

relative to the center of the window function Q_z^0. Equation (7.2) shows that there is a broadening of the intrinsic effective interfacial density along the surface normal direction due to the finite extent of the reciprocal space window function $\hat{W}_{1D}(Q_z)$ multiplied by a phase factor $\exp[-iQ_z^0 z]$:

$$\rho_{\text{eff-0}}(z) = \left\{\sum_{n=0}^{\infty}\beta^n\delta(z+nc_s)\otimes_z \exp\left[-iQ_z^0 z\right]\Delta Q_z \text{sinc}\left(\frac{\Delta Q_z}{2}z\right)\right\}$$
$$= \Delta Q_z \exp\left[-iQ_z^0 z\right]\sum_{n=0}^{\infty}\beta^n \exp\left[-iQ_z^0 nc_s\right]\text{sinc}\left[\frac{\Delta Q_z}{2}(z+nc_s)\right]. \quad (7.3)$$

The intrinsic effective density consists of the resolution broadened densities for each layer multiplied by the phase factor $\exp[-iQ_z^0 nc_s]$, corresponding to the vertical phase shift for that layer, at $z = -nc_s$ with respect to an interface at $z = 0$, and then summed over all layers. The term β^n, accounting for the attenuation of the x-ray beam into the substrate, ensures convergence of the expression. There is also an overall prefactor $\exp[-iQ_z^0 z]$, which is the complement to the prefactor in Eq. (2) associated with the use of FFTs.

The function $\rho_{\text{eff-0}}$ is the mechanism by which CXR measurements obtain interfacial specificity, as described previously [34]. This derives from the prefactor that imposes a different phase for each layer which leads to destructive interference between the individual atomic layers. Its detailed behavior depends upon both the vertical location and size of the reciprocal space window function, defined by Q_z^0 and ΔQ_z, respectively. This is shown in Fig. 2, calculated for the case of $\Delta Q_z = 0.05 Q_B$, where the substrate Bragg peak is at $Q_B = 2.09\ \text{Å}^{-1}$, so that the window function excludes the substrate Bragg peak (using $\beta = 0.99$). The sinc function for each layer is much wider than the layer spacing because it is controlled by the vertical resolution $2\pi/\Delta Q_z$. The phase shift between neighboring layers [Fig. 2(a)] leads to destructive interference for all layers that are far from the interface, resulting in an effective density that is nonzero in magnitude only near the interface and with a finite width along the surface normal direction [Fig. 2(b)]. Note also that the observed behavior is independent of the magnitude of β if the decay length is larger than the effective interfacial width (i.e., $\beta > 0.9$). The result is also independent of the number of layers included in the summation N as long as $\beta^N \sim 0$. For the case of $\beta = 1$ (i.e., no attenuation), the expression predicts a second peak at $z = -\text{Nc}$, corresponding to the scattering from the bottom layer of a N-layer thick crystal, at which point the CTR shape will include oscillations in the structure factor magnitude. These properties of $\rho_{\text{eff-0}}$ for different values of β are illustrated in Fig. S1 of the Supplemental Material [39].

The magnitude of the intrinsic effective density $|\rho_{\text{eff-0}}|$ has a shape that is similar to the sinc function for a single layer, with a maximum magnitude located at the surface height, and with the expected nodes of the sinc function being replaced by intensity minima [Fig. 2(b)]. The phase of the intrinsic effective density reveals an internal vertical phase gradient [indicated both in color in Fig. 2(b) and plotted in Fig. 2(c)]. Note that the width of this function is controlled by the experimental vertical real-space resolution as might be expected due to the sharp cutoff of the vertical window function $\hat{W}_{1D}(q_z)$. This result can be understood from Eq. (6.2) which shows that the vertical shape of $\rho_{\text{eff-0}}$ is the convolution of the semi-infinite substrate electron density with the vertical real-space resolution function, i.e., the sinc function arising from the vertical cropping of the data in the reciprocal space; thus, the effective density retains characteristics of both the sinc function associated with the data termination and a phase gradient that is the result of the vertical asymmetry of the CTR.

E. Full expression for the effective interfacial density $\rho_{\text{eff}}(x)$

The final expression for the effective interfacial density can now be written out explicitly [Eq. (8)]. Here we make use of the observation that the vertical width of the intrinsic effective density $\rho_{\text{eff-0}}$ is controlled by resolution along the surface normal direction and is much broader than the unit-cell electron density. Consequently, we replace that convolution with the average unit-cell density $\langle\rho_{\text{UC}}\rangle$:

$$\rho_{\text{eff}}(\boldsymbol{x}) = \langle\rho_{\text{UC}}\rangle\left\{A_{2D}(x,y)\exp\left[iQ_z^0 h(x,y)c_s\right]\right.$$
$$\left.\times\ \rho_{\text{eff-0}}[z - h(x,y)c_s]\right\}\otimes_x W_{2D}(x,y). \quad (8)$$

This effective interfacial density is described by a complex-valued function $\rho_{\text{eff}-0}[z-h(x,y)c_s]$, whose magnitude is peaked at the interface height $h(x,y)$, along with a phase prefactor corresponding to the interfacial height $\exp[iQ_z^0 h(x,y)c_s]$. Although $\rho_{\text{eff-0}}[z-h(x,y)c_s]$ is complex valued, its value is the same at $z = h(x,y)c_s$, for any (x,y).

F. Asymptotic behavior of the intrinsic effective density $\rho_{\text{eff-0}}(z)$

A deeper understanding of the complex interfacial density can be obtained by deriving an approximate expression from the definite integral over the range defined by the reciprocal space window function:

$$\rho_{\text{eff-0}}(z) = \exp\left[i\,Q_z^0 z\right]\int_{Q_z^0-\frac{\Delta Q_z}{2}}^{Q_z^0+\frac{\Delta Q_z}{2}}\frac{\exp(-iQ_z z)}{1-\exp(-iQ_z c_s)}dQ_z$$
$$= \int_{-\frac{\Delta Q_z}{2}}^{\frac{\Delta Q_z}{2}}\frac{\exp(-iq_z z)}{1-\exp(-iq_z c_s)\exp\left(-iQ_z^0 c_s\right)}dq_z, \quad (9.1)$$

where the second expression uses the reduced momentum transfer $q_z = Q_z - Q_z^0$. We ignore the role of beam attenuation β [from Eq. (4.3)] as we have demonstrated that $\rho_{\text{eff-0}}(z)$ is independent of β for the conditions that we are considering [39]. A linear Taylor expansion of the denominator for small

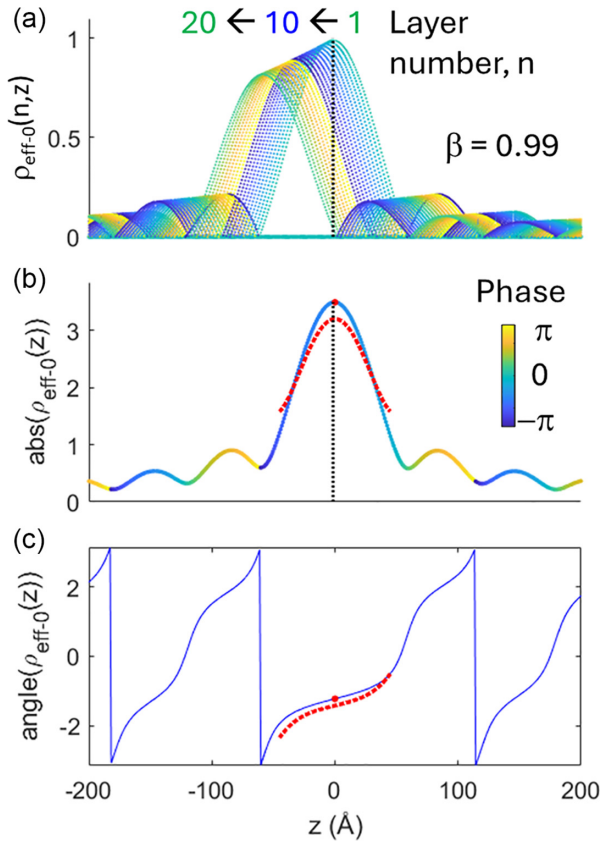

FIG. 2. (a) The intrinsic effective density $\rho_{\text{eff-0}}(z)$ is calculated by representing the nth substrate layer as a sinc function, $\text{sinc}[\frac{\Delta Q_z}{2}(z+(n-1)c_s)]$, for $n=1,2,\ldots$. Here, the sinc functions for the first 20 layers of a semi-infinite substrate (with the surface at $z=0$, vertical black dashed lines) are shown with its amplitude along the vertical axis and the phase indicated in color [in radians; scale bar for phase is shown, inset, in (b)]. A beam attenuation of $\beta=0.99$ for each layer is included [leading to the decrease in the peak density for layers 1–20, as shown in (a)]. The intrinsic effective density $\rho_{\text{eff-0}}(z)$ as its (b) magnitude and (c) phase, corresponding to the sum of all layers ($n=1$ to ∞), are shown. Also in (b) and (c) are the asymptotic behaviors of the amplitude and phase obtained by a Taylor expansion [red dashed line; as described by Eq. (9.3)]. The red dots indicate the height corresponding to the maximum effective density amplitude (where the amplitude and phase of the effective density are evaluated).

values of q_z leads to the result

$$\rho_{\text{eff-0}}(z) \approx \left[\frac{\Delta Q_z}{1-\exp\left(-iQ_z^0 c_s\right)}\right]\left\{\text{sinc}\left(\frac{\Delta Q_z}{2}z\right)-\frac{1}{12}\times\frac{c_s\exp\left(-iQ_z^0 c_s\right)}{\left[1-\exp\left(-iQ_z^0 c_s\right)\right]}{\Delta Q_z}^2 z\right\}. \tag{9.2}$$

Equation (9.2) shows that intrinsic effective density has three primary contributions. The overall magnitude is determined by the prefactor which is controlled by both ΔQ_z and Q_z^0 (i.e., where the reflectivity signal is measured on the CTR and how much of the CTR is included in the measurement). The first term within the curly brackets is a real-valued sinc function located at $z=0$ (corresponding to the surface height) whose width is controlled by the vertical data range (i.e., the resolution). This indicates that a dominant contribution to the shape of $\rho_{\text{eff-0}}(z)$ is determined by the choice of the data range ΔQ_z. The second contribution to the density is described by a term that is linear in z whose prefactor depends again upon both Q_z^0 and ΔQ_z. In this expression, both terms in the curly brackets and the prefactor are complex valued.

The limiting behavior for the intrinsic effective density, measured near a substrate Bragg peak, leads to the expression

$$\rho_{\text{eff-0}}(z) \approx \frac{\Delta Q_z}{i\left(Q_{\text{B}}-Q_z^0\right)c_s}\left\{\text{sinc}\left(\frac{\Delta Q_z}{2}z\right)+\frac{i{\Delta Q_z}^2 z}{12\left(Q_{\text{B}}-Q_z^0\right)}\right\}. \tag{9.3}$$

This shows that the linear contribution to the intrinsic effective density is purely imaginary near the substrate Bragg peaks where the reflectivity signal becomes largest, corresponding to a vertical phase gradient within the interfacial region. The inverse dependence on $(Q_{\text{B}}-Q_z^0)$ shows that the phase gradient will be maximized for measurements near the substrate Bragg peak (where the reflectivity signal varies most rapidly with Q_z) and increases quadratically with size of the reciprocal space window function ΔQ_z. The behavior described by Eq. (9.3) [red lines in Figs. 2(b) and 2(c)] is compared to the exact functional form predicted by Eq. (7.3). Note that the predicted phase variation is nonlinear even though this expression includes only the first linear term in the Taylor expansion. This is due to the nonlinear variation of the real part of $\rho_{\text{eff-0}}(z)$ described by the sinc function.

III. SIMULATED CXR MEASUREMENTS

A. Kinematics and coordinate transformations

CXR measurements are simulated by illuminating a crystalline surface with a finite-sized coherent x-ray beam at an angle of incidence θ (with respect to the surface plane) and placing the detector in a specular reflection condition, at an angle 2θ, whose value is twice the incident angle corresponding to a vertical momentum transfer $\boldsymbol{Q}=Q_z^0$ (Fig. 1). Data are obtained by rocking the sample (i.e., changing the incident angle θ with respect to the incoming beam) over a narrow angular range ($\sim 1^\circ$) with small angular steps ($\delta\theta\sim 0.001^\circ$) with a fixed detector to ensure oversampling within the surface plane. This registers a series of slices across the CTR so that a 3D volume of diffracted intensity is measured [30,34,38]. The Ewald sphere is tilted, however, with respect to the surface normal direction leading to a nonorthogonal ROI volume [Figs. 1(c), 1(d), and 3(a-iii)].

The relevant details associated with CXR measurements will be illustrated here by simulation. This is done by calculating the effective density using the following expression:

$$\rho_{\text{eff}}(\boldsymbol{x}) = \text{FFT}^{-1}[\{\mathcal{FT}[\text{A}_{\text{3D}}(\boldsymbol{x})] \otimes [F_{\text{top}}(\boldsymbol{Q})F_{\text{col}}(Q_z)]\}\hat{W}_{\text{3D}}(\boldsymbol{Q})]. \tag{10}$$

Here, $F_{\text{top}}(\boldsymbol{Q})$ is calculated as a discrete Fourier transform of the interfacial topographic phase [Eq. (4.4)], $\exp[iQ_z^0 h(x,y)c]$, for the specific choice of reciprocal space ROI. This calculation assumes a unit cell with pointlike

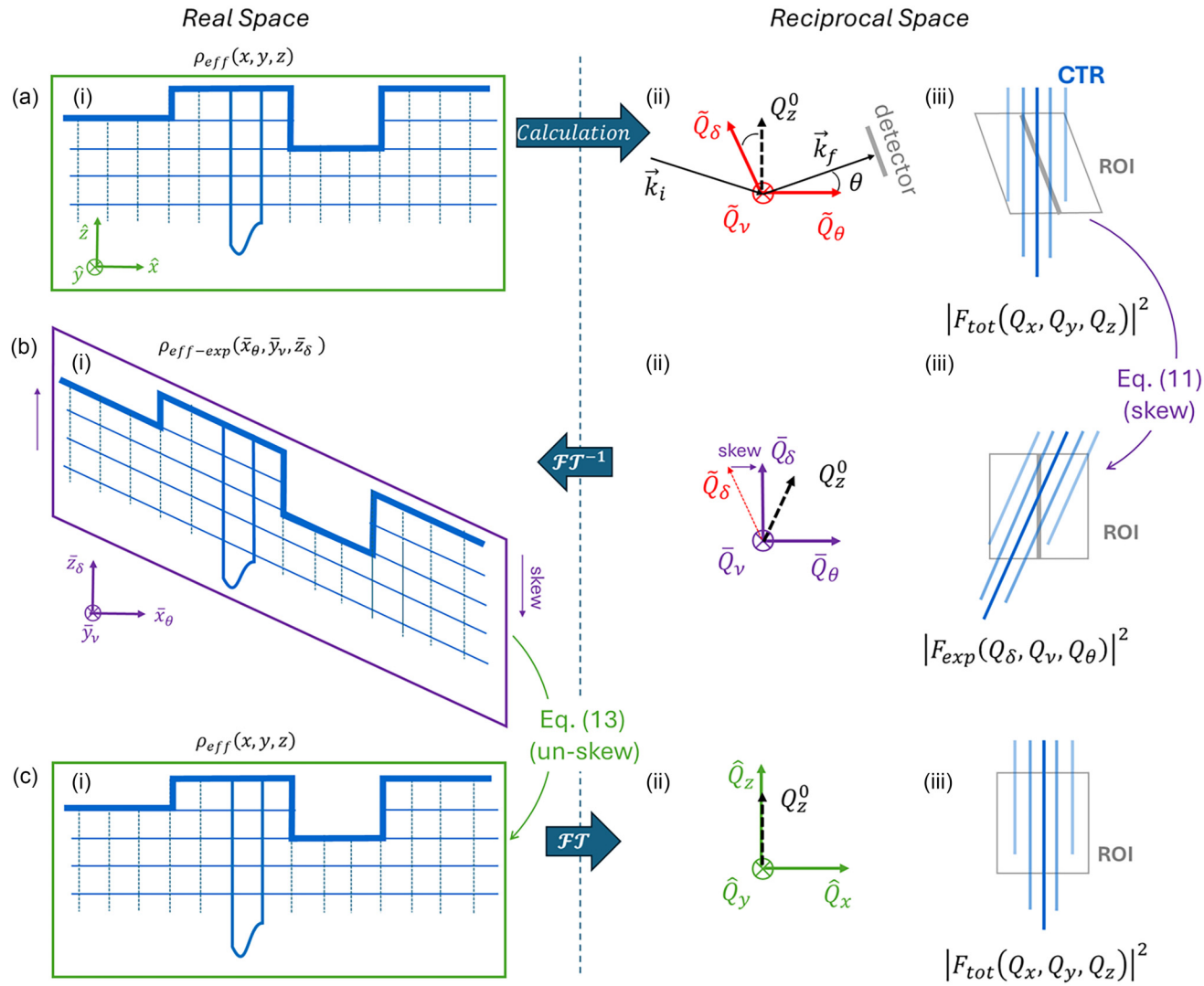

FIG. 3. Conjugate reference frames in real and reciprocal space for the simulations. (a) The orthogonal reference frame of (i) the sample surface, (ii) the coordinate geometry of the measurement and the directions defined by the detector plane (Q_δ, Q_ν), and the scan direction (Q_θ), and (iii) the intensities calculated from the sample in the orthogonal frame with the nonorthogonal experimental ROI (gray parallelogram with a thick gray line indicating the detector plane at the center of the ROI). (b) Data represented in (iii) the "square matrix representation" that is used by standard phase retrieval algorithms correspond to skewing the (ii) reciprocal space and real-space coordinates where the detector plane is along the vertical direction. Thus, the detector slices appear as vertical slices and, as a result, the CTR appears tilted; (i) the effective densities are obtained by inverse Fourier transform of the CXR and result in a recovered density that is vertically skewed with respect to the original object. (c) The original structure in the orthogonal reference frame is recovered by use of a skewing operator [Eq. (13)], whose Fourier transform corresponds to the structure factor within the orthogonal ROI.

atoms (inclusion of the atomic structure of the substrate, including the finite size of the atoms and their arrangement within the unit cell, can be incorporated using atomic and unit-cell form factors [29]). The ideally terminated interface has a column form factor corresponding to the ideal CTR form factor for $F_{\rm col}(Q_z) = F_{\rm CTR}(Q_z)$, which is calculated in closed form [Eq. (4.3)]. We consider the specific case of specular reflectivity from an ideally terminated orthogonal lattice. The extension to the general situation is straightforward and involves only different choices for $F_{\rm col}(Q_x, Q_z)$ (for instance, to account for any nonideal terminations, nonorthogonal crystal structures, and nonspecular scattering conditions).

The oblique illumination of the surface in a specular reflection geometry with a finite beam size has multiple distinct effects on the effective density. The first effect of beam illumination is the explicit inclusion of the beam direction in the calculation of the intensities. We assume the beam has a Gaussian profile transverse to the beam direction characterized by a full width at half-maximum Δ_b, and the total structure factor is calculated in the orthogonal coordinates of the interface [Fig. 3(a-i)]. This extends the beam footprint laterally within the scattering plane and laterally shifts the beam illumination for each layer below the surface. This convolution of the beam with the interfacial structure is calculated by Fourier transform: $A(\boldsymbol{Q}) \otimes F(\boldsymbol{Q}) = \mathcal{FT}^{-1}[\mathcal{FT}[A]\mathcal{FT}[F]]$. Note that

a large ROI [dashed white line, Fig. 1(c)] that is twice the size of the experimental ROI [solid red line, Fig. 1(c)] is used in the structure factor calculations to avoid artifacts associated with the convolution and skewing to simulate realistic signals.

The second effect of the incident beam direction is found in the shape of the reciprocal space ROI volume $\hat{W}_{3D}(\boldsymbol{Q})$. For a measurement in the specular reflection geometry, the ROI is nonorthogonal because the Ewald sphere (the range of intensities probed at a fixed sample position) is tilted with respect to the surface normal direction by an angle corresponding to the angle of incidence θ [red box, Fig. 1(c), and gray box, Fig. 3(a-iii)]. Consequently, the ROI is defined along the vectors Q_δ and Q_ν within the detector plane, and Q_θ along the rocking scan direction [where δ and ν are the corresponding scattering angles across the detector, within and transverse to the scattering plane, respectively; θ is the angle corresponding to the direction of the rocking scan, Fig. 3(a-ii)]. Here, we assume that the lateral ROI range in Q_x and Q_y is sufficiently large so that the CTR has a sharp cutoff along Q_z but not in (Q_x, Q_y).

Measured CDI data are typically analyzed as a stack of detector images obtained in a rocking scan. This "square matrix representation" is an orthogonal basis in which the detector plane is oriented in the vertical direction and the rocking curve scan direction is in the horizontal direction [gray lines, Fig. 3(b-iii)]. In this basis the CTR is tilted due to a shear distortion of the structure factor in the Q_θ direction (i.e., along the rocking curve direction), which in this measurement geometry coincides with Q_x [Fig. 3(b-ii)]. The effect on the measurement is incorporated by calculating the total structure factor $F_{tot}(\boldsymbol{Q})$, within a large ROI, and then skewing these values (about the center of the ROI, Q_z^0) onto the orthogonal ROI [Fig. 3(b-iii)], corresponding to $F_{exp}(\boldsymbol{Q})$:

$$F_{exp}(\boldsymbol{Q}) \equiv \mathcal{FT}_x\left\{\exp\left[i\left(Q_z - Q_z^0\right)x\tan(\theta)\right]\mathcal{FT}_x^{-1}[F_{tot}(\boldsymbol{Q})]\right\}. \tag{11}$$

The operator $\exp[i(Q_z - Q_z^0)x\tan(\theta)]$ was derived using the formalism developed by Maddali *et al.* [40,41] to simulate the effect of a nonorthogonal ROI [see the Supplemental Material for a rigorous derivation of Eq. (11) [39] and see Refs. [37,40,41], cited therein]. The experimentally observed effective density is then calculated by inverse FFT of these simulated data using an orthogonal ROI, $\hat{W}_{3D\text{-}orth}(\boldsymbol{Q})$:

$$\rho_{eff\text{-}exp}(\boldsymbol{x}) = \mathrm{FFT}^{-1}[F_{exp}(\boldsymbol{Q})\hat{W}_{3D\text{-}orth}(\boldsymbol{Q})]. \tag{12}$$

A direct consequence of the nonorthogonal ROI is that the direct space interfacial image of $\rho_{eff\text{-}exp}(\boldsymbol{x})$ obtained with Eq. (12) is distorted in real space [Fig. 3(b-i)]. An undistorted version of the effective density can, thus, be recovered from that obtained from $\rho_{eff\text{-}exp}(\boldsymbol{x})$ by the following relation [40,41]:

$$\rho_{eff}(\boldsymbol{x}) = \mathcal{FT}_{\mathbf{z}}^{-1}\left\{\exp\left[-i\left(Q_z - Q_z^0\right)x\tan(\theta)\right] \times \mathcal{FT}_{\mathbf{z}}\{\rho_{eff\text{-}exp}(\boldsymbol{x})\}\right\}. \tag{13}$$

This confirms that the imaged interfacial density obtained from a ROI that is skewed due to the tilt of the Ewald sphere [i.e., $\rho_{eff\text{-}exp}(\boldsymbol{x})$] is skewed with respect to the actual interfacial structure $\rho_{eff}(\boldsymbol{x})$, but is otherwise equivalent to the effective density obtained using an orthogonal ROI. This expression allows an unskewed image of the interface to be recovered when using the nonorthogonal ROI corresponding to an actual experiment [Fig. 3(c-i)]. The Fourier transform of $\rho_{eff}(\boldsymbol{x})$ will then reproduce the intensities within the orthogonal ROI [Fig. 3(c-iii)]. Recall that the derivation of this formalism assumed that the x-ray beam was incident on the surface at normal incidence. The differences in the effective densities obtained using the orthogonal and skewed ROIs correspond to the differences in scattering intensities for x-ray beams that are incident at normal vs oblique angles of incidence. Therefore, the simplifying assumption of using a normal incident beam that was made in the derivation Eq. (6.1) does not limit the generality of the derived results in Eq. (8).

B. Recovering the topography from simulated CXR

These ideas are illustrated in Fig. 4. For these calculations, we incorporate the details of a measurement that are comparable to what might be accessed for measurements with hard x-ray beams (e.g., $E = 10$ keV). These calculations assume a parallel fully coherent beam having a Gaussian profile with a full width at half-maximum (FWHM) of 0.5 μm. The surface is assumed to be crystalline having a vertical and lateral lattice spacing of $a_s = c_s = 3$ Å, with a vertical Bragg peak position of $Q_B = 2\pi/c_s = 2.09$ Å^{-1}. The simulated measurements correspond to a vertical momentum transfer of $Q_z^0 = 0.95\,Q_B = 1.99$ Å^{-1} at an incident angle of $\theta = 11.3^\circ$ and a beam footprint within the scattering plane of 2.5 μm. These simulated results will be compared to equivalent calculations near the CTR midzone, at $Q_z^0 = 0.55\,Q_B = 1.15$ Å^{-1} and $\theta = 6.5^\circ$. In both cases, we include a reciprocal space ROI that has size of $\Delta Q_z = \Delta Q_x = 0.01 Q_B = 0.021$ Å^{-1} in both the vertical and horizontal directions, respectively. This corresponds to a spatial resolution of $2\pi/\Delta Q = 30$ nm. The assumed surface topography [Figs. 1(a) and 1(b)] includes a series of steps with heights of 1–4 vertical unit cells, separated by flat terrace areas.

The calculated intensities within the large ROI [Fig. 4(a-ii)] show the expected specular truncation rod as a function of reduced vertical momentum transfer (e.g., $q_z = Q_z - Q_z^0$) along with diffuse scattering that appears as speckles (for $|q_x| > 0$) due to the presence of steps. Fourier transform of the complex structure factors within the orthogonal ROI [white box, Fig. 4(a-ii)] reveals the effective density magnitude [Fig. 4(a-i)] which is concentrated in a single plane near $z = 0$. It has a lateral variation that reflects the beam illumination and a vertical width corresponding to a single pixel whose size is defined by vertical resolution, as expected from theory. This confirms the main predictions of the theoretical formalism [Eq. (8)] and previous simulations [34]. These amplitude data do not reveal any clear sensitivity to the topography since the height range of the topography (~4 unit cells, or 1.2 nm) is much smaller than the resolution (30 nm) corresponding to the pixel size.

The same analysis is also applied to simulated experimental data derived using the nonorthogonal ROI corresponding to a measurement [red box, Fig. 4(a-ii)] where the CTR appears tilted [Fig. 4(b-ii)]. In this case, the vertical slices within the red ROI correspond to detector images in an experiment (the extension of the signal outside the ROI is not physically

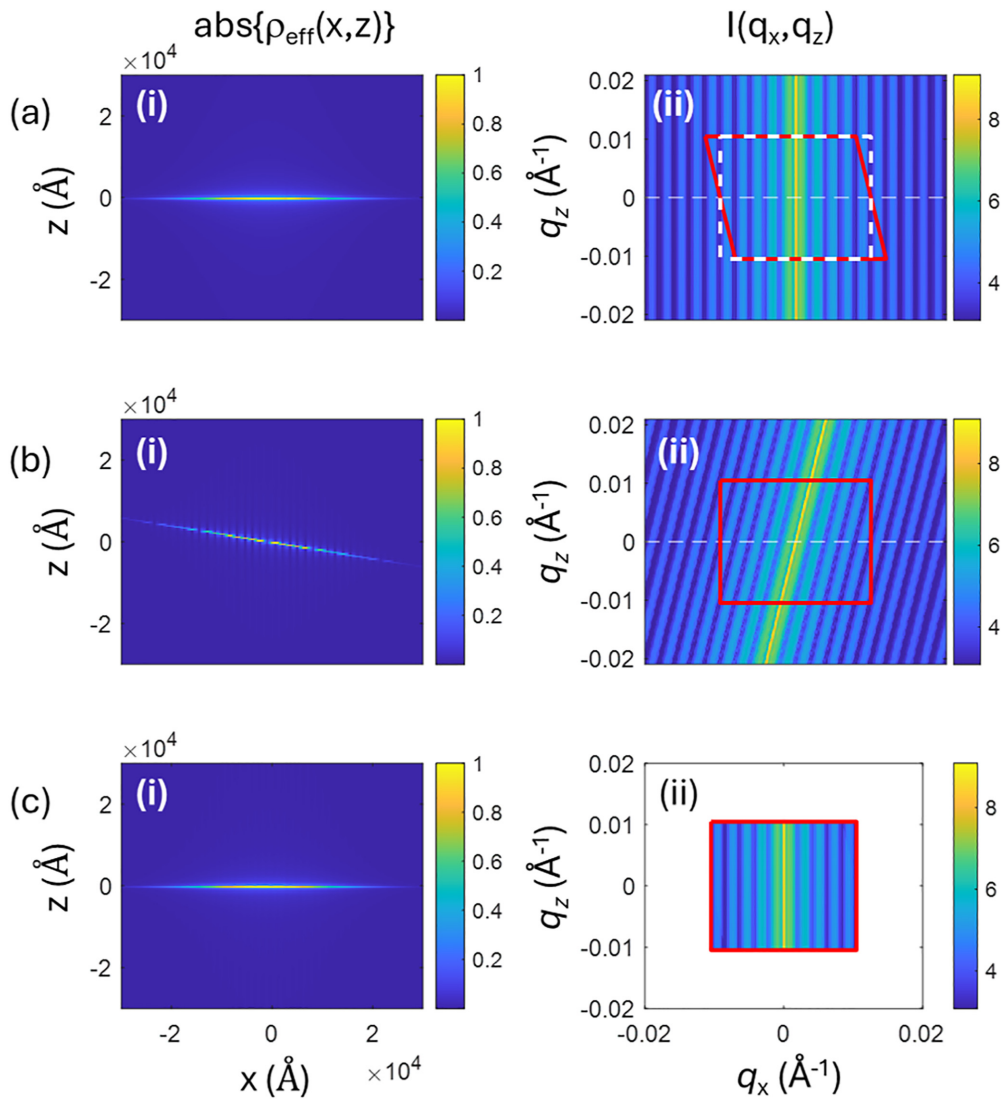

FIG. 4. (a) The magnitude of (i) the effective density $\rho_{\text{eff}}(x, z)$ and (ii) the associated intensities (as $\log_{10}[\text{I}(Q_x, Q_z)]$) are shown for the data within the large ROI, including the orthogonal ROI (white dashed line) and the experimental ROI (red parallelogram). Here the surface plane is at $z = 0$. (b) The data are skewed to map the structure factors from the orthogonal reference frame (a-ii) onto the square matrix representation (b-ii), whose Fourier transform leads to a tilted interface. (c) The original density is recovered (c-i), after skewing the effective density (b-i), whose Fourier transform is shown (c-ii). (Note the absence of intensities in the white regions.)

meaningful and is shown to illustrate the skewing process). The real-space image of the effective density becomes tilted, as expected [Fig. 4(b-i)]. Understanding the surface height and phase behavior of these images would be complicated by the pixelization of the effective density and its misalignment with respect to the surface coordinate frame. We then use the skewing operator [Eq. (13)] to obtain an image of the effective density [Fig. 4(c-i)] that appears identical to that obtained from the orthogonal ROI. As expected, the intensities obtained by Fourier transform of the effective densities recover the original intensities within the ROI [Fig. 4(c-ii)].

We now directly test the derived formalism by comparing the assumed beam illumination and surface topography with that extracted from the effective densities (Fig. 5). Here, an image of the magnitude, abs(ρ_{eff}) [Fig. 5(a-i)] and phase, angle (ρ_{eff}) [Fig. 5(a-ii)] of the effective density (for $Q_z^0 = 0.95\, Q_{\text{B}}$, as shown in Fig. 4) are shown over a narrower range of heights so that their properties can be discerned. The lateral variation of the amplitude within the interfacial plane [dashed line, Fig. 5(a-i)] shows the expected Gaussian shape of the beam illumination except for small deviations near the steps [Fig. 5(a-iii)]. These features resemble the features observed in x-ray reflection interface microscopy (XRIM) measurements of interfacial topography [32,33]. XRIM is an incoherent imaging tool that probes only the amplitude of the interfacial structure factor. Its sensitivity to step height, imaged as the local change in the imaged amplitude across the step, has been shown to be due to interference associated with the change in phase at the step [32,33].

The effective density phase (shown where the effective density amplitude is larger than 10% of the maximum value) shows both lateral and vertical structure [Fig. 5(a-ii)]. The lateral variation of the phase is due to the presence of

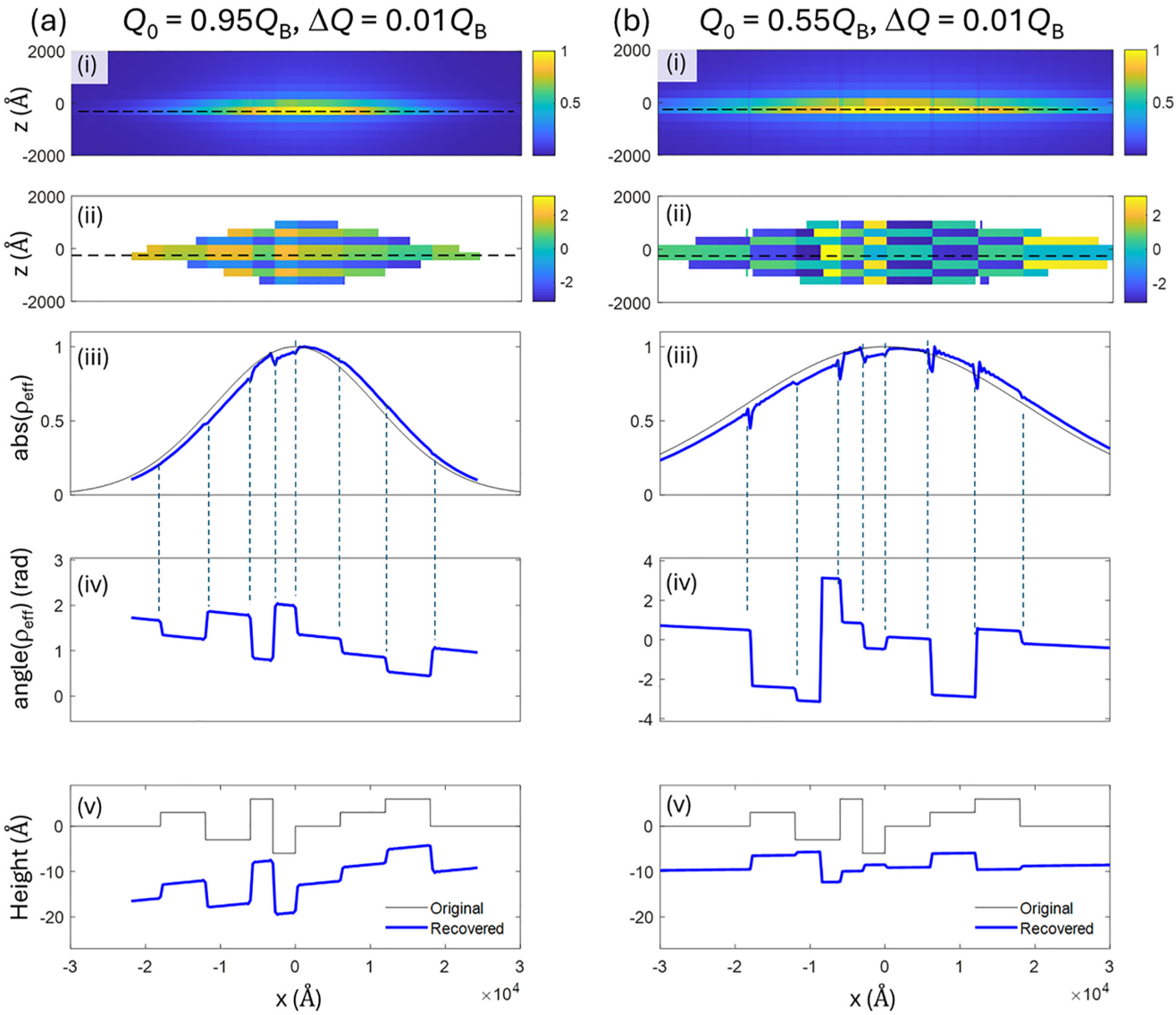

FIG. 5. Comparison of the original and recovered effective densities for two scattering conditions: (a) $Q_z^0 = 0.95\,Q_B$ and (b) $Q_z^0 = 0.55\,Q_B$, both using a ROI of size $\Delta Q_z = \Delta Q_x = 0.01 Q_B$. For each scattering condition, the (i) amplitude and (ii) phase of the effective density are shown by inverse Fourier transform of the complex structure factor. The (iii) amplitude and (iv) phase of the complex effective densities (blue lines) are obtained from the plane of maximum effective density [dashed lines in (i) and (ii), respectively]. (v) The topography is recovered from the phase using Eq. (14). The vertical dashed lines between (iii) and (iv) show how discontinuities in the recovered amplitudes correspond to the step locations. The recovered amplitudes and heights (blue lines) are also compared to that from the original structure [gray lines in (ii) and (v)], demonstrating agreement for the amplitudes in each case while the actual topography (i.e., step heights) is recovered in (a) but not (b).

steps, $\exp[iQ_z^0 h(\boldsymbol{x})c_s]$, as expected from Eq. (8). This can be quantified by plotting the phase within the surface plane [Fig. 5(a-iv)] at the vertical position corresponding to the maximum in the effective density magnitude. The phase of the complex effective density shows direct sensitivity to the topography [Fig. 5(a-iv)], with changes in phase occurring at the location of the steps and coinciding with weaker changes in amplitude. The surface height profile $h(x)$ can be recovered from the phase using the relation

$$h(x, y) = [\text{angle}(\rho_{\text{eff}}) + 2\pi n]/\left[\left(Q_z^0 - Q_B\right)c_s\right] \qquad (14)$$

with a corresponding surface height $h(x, y)c_s$. The term 2πn indicates that the recovered phase is only known to within integer multiples of 2π (i.e., there is a modulo-2π uncertainty in the recovered phase). The recovered surface topography is shown [using $n = 0$ in Eq. (14)] and reproduces the original topography except for an overall offset in height (which is not uniquely observed) and a small gradient in the height (which is not understood). This example shows that the surface topography can be observed directly by CXR even when the vertical height variation is substantially smaller than the vertical resolution of the measurement.

Results for a second simulation with the same topography but at $Q_z^0 = 0.55\,Q_B$ are shown in Fig. 5(b). The effective density amplitude [Fig. 5(b-i)] is very similar to that observed at $Q_z^0 = 0.95\,Q_B$ [Fig. 5(a-i)] but with a larger lateral

footprint due to the smaller incident angle, and with larger changes in the amplitude at the steps, shown explicitly [Fig. 5(b-iii)], consistent with the interpretation for XRIM [32,33]. The phase of the effective density shows larger changes across the image [Fig. 5(b-ii)] and is evident in a plot of the lateral variation of the recovered phase within the surface plane [Fig. 5(b-iii)] which is generally larger in magnitude from that observed at $Q_z^0 = 0.95\,Q_\mathrm{B}$ [Fig. 5(a-iii)] as expected due to the higher phase sensitivity of the CXR data at the midzone of the CTR. The derived height profile recovers the expected step locations but does not, however, recover the actual terrace heights. Furthermore, the recovered topography has apparent step heights that are not multiples of $c_s = 3$ Å as expected for a crystal surface. In fact, in many cases the apparent step height is smaller than the assumed vertical lattice spacing which is unphysical. We note that the differences between the actual and recovered profiles have values of approximately ~ 6.3 Å $= 2\pi/(Q_z^0 - Q_\mathrm{B})$, reflecting the modulo-$2\pi$ ambiguity indicated in Eq. (14). This is an artifact of deriving the surface height from the measured phase which can lead to inherent ambiguities in the derived height, as is discussed more below.

C. Comparison of recovered and predicted effective densities

Since the intensities along the surface normal direction are inherently diffuse (i.e., they appear as vertical streaks for any measurement that does not include the substrate or thin-film Bragg peaks), the observed effective density will be "resolution limited" along that direction, and therefore will have a vertical width of approximately a single pixel when sampled at the real-space spacings corresponding to the data range. The theoretical formalism [e.g., Eqs. (9.2) and (9.3)] predicts that the phase of the effective density has an inherent vertical gradient that occurs within its vertical width. This prediction can be tested by Fourier interpolation of the effective density for length scales smaller than the resolution:

$$\rho_{\text{eff-interp}}(\boldsymbol{x}) = \mathcal{FT}_z^{-1}\{\mathcal{FT}_z[\rho_\text{eff}(\boldsymbol{x})]_m\}_{bm}. \tag{15}$$

Here, m indicates the size of the matrix $\rho_\text{eff}(\boldsymbol{x})$ along the vertical direction, while the size of the interpolated density is increased by a padding $\mathcal{FT}_z[\rho_\text{eff}(\boldsymbol{x})]$ with zeros by a factor of b before the final Fourier transform.

The interpolated effective density is shown in Fig. 6(a) for the calculation at $Q_z^0 = 0.95\,Q_\mathrm{B}$. Its amplitude shows the expected sinc function shape in the vertical direction [Fig. 6(a-ii)] with a vertical width controlled by the resolution ($\sim$30 nm). The phase reveals the presence of a gradient in the phase as a function of z, as well as shifts in the vertical phase associated with changes in the surface height [Fig. 6(a-iii)]. These observations are consistent with the predictions by theory [Eqs. (7.3), (8), and (9.3)], and as illustrated in Fig. 2. The important role of phase sensitivity in recovering surface topography can be seen by plotting the vertical variation of the amplitude and phase of the effective density for two positions separated by a surface step (Figs. 6(a-iv) and 6(a-v)]. These data show that the change in surface height as measured by a shift in the effective density amplitude is negligible, as expected since the changes in height are much smaller than the resolution. However, the changes in phase at the surface location, defined at the height of maximum amplitude [dashed line, Figs. 6(c) and 6(d)] is significant and a direct consequence of the change in surface height. Similar results are shown for the simulation of the effective density at $Q_z^0 = 0.55\,Q_\mathrm{B}$ [Fig. 6(b)], which are qualitatively similar to those observed in Fig. 6(a), except for a higher sensitivity in the phase changes associated with steps.

D. Considerations for obtaining unique topographies

The sensitivity to interfacial topography derives from two sources: the vertical shift in the effective density amplitude and the change in phase of the effective density. Since a typical measurement will have a ROI whose size is significantly smaller than the Bragg peak spacing, the vertical resolution will typically be inherently large ($\sim$10's of nm). While this provides high resolution with respect to the typical beam footprint ($\sim$few microns), it is large compared to the relevant topographic variation, except for very rough surfaces. We have shown, however, that the phase sensitivity is sufficient to recover elementary topography through the changes in phase for an ROI at $Q_z^0 = 0.95\,Q_\mathrm{B}$, but that the recovered topography for an ROI at $Q_z^0 = 0.55\,Q_\mathrm{B}$ includes unphysical step heights.

One consideration in this regard is that the recovered phase is uncertain to any multiple of 2π (the "modulo-2π ambiguity"). Since what is observed for surfaces with well-separated steps is the phase change between different terraces, this modulo-2π ambiguity can lead to multiple heights that are consistent with the observed phase at each position that differ by multiples of $\Delta z_{\text{mod-}2\pi} = 2\pi/(Q_z^0 - Q_\mathrm{B})$, where Q_B is the momentum transfer of the closest Bragg peak. This relation makes use of the observation that the topographic phase of the effective density at $Q = Q_\mathrm{B}$ corresponds to $2\pi h(x)$ which is indistinguishable from any multiple of 2π. This uncertainty is inherent to any phase-based approach that is derived from measurements at a single momentum transfer (e.g., as in Bragg x-ray standing waves which probe the structure factor phase at the Bragg peak position [42–44]). The interface location, however, is independently constrained by the magnitude of the effective density, and this sensitivity derives from measuring the structure factor within the extended ROI width ΔQ_z, leading to a resolution broadened width $\Delta z_\text{res} = 2\pi/\Delta Q_z$, providing a distinct (albeit lower resolution) constraint on the surface height. Therefore, a unique determination of terrace heights can be obtained when the modulo-2π ambiguity $\Delta z_{\text{mod-}2\pi} = 2\pi/(Q_z^0 - Q_\mathrm{B})$ is comparable to (or larger than) the vertical resolution $\Delta z_\text{res} = 2\pi/\Delta Q_z$. This implies that a design criterion for obtaining unique topographies is that $\Delta z_{\text{mod-}2\pi} \gtrsim \Delta z_\text{res}$. It is also necessary to exclude the Bragg peak to retain interfacial specificity, which provides a second constraint. Together, these considerations reveal that the optimal scattering conditions to obtain a unique topography should be chosen based on the constraints

$$\Delta Q_z/2 < \left|Q_z^0 - Q_\mathrm{B}\right| \lesssim \Delta Q_z. \tag{16}$$

This insight reveals that a unique measurement of the surface topography with a given ROI size will be best achieved when the ROI is adjacent to a Bragg peak.

This explains the differences in recovered topographies derived from inversion of simulated data at $Q_z^0 = 0.95\,Q_\mathrm{B}$ [Fig. 5(a-v)] and $Q_z^0 = 0.55\,Q_\mathrm{B}$ [Fig 5(b-v)] for a fixed $\Delta Q_z =$

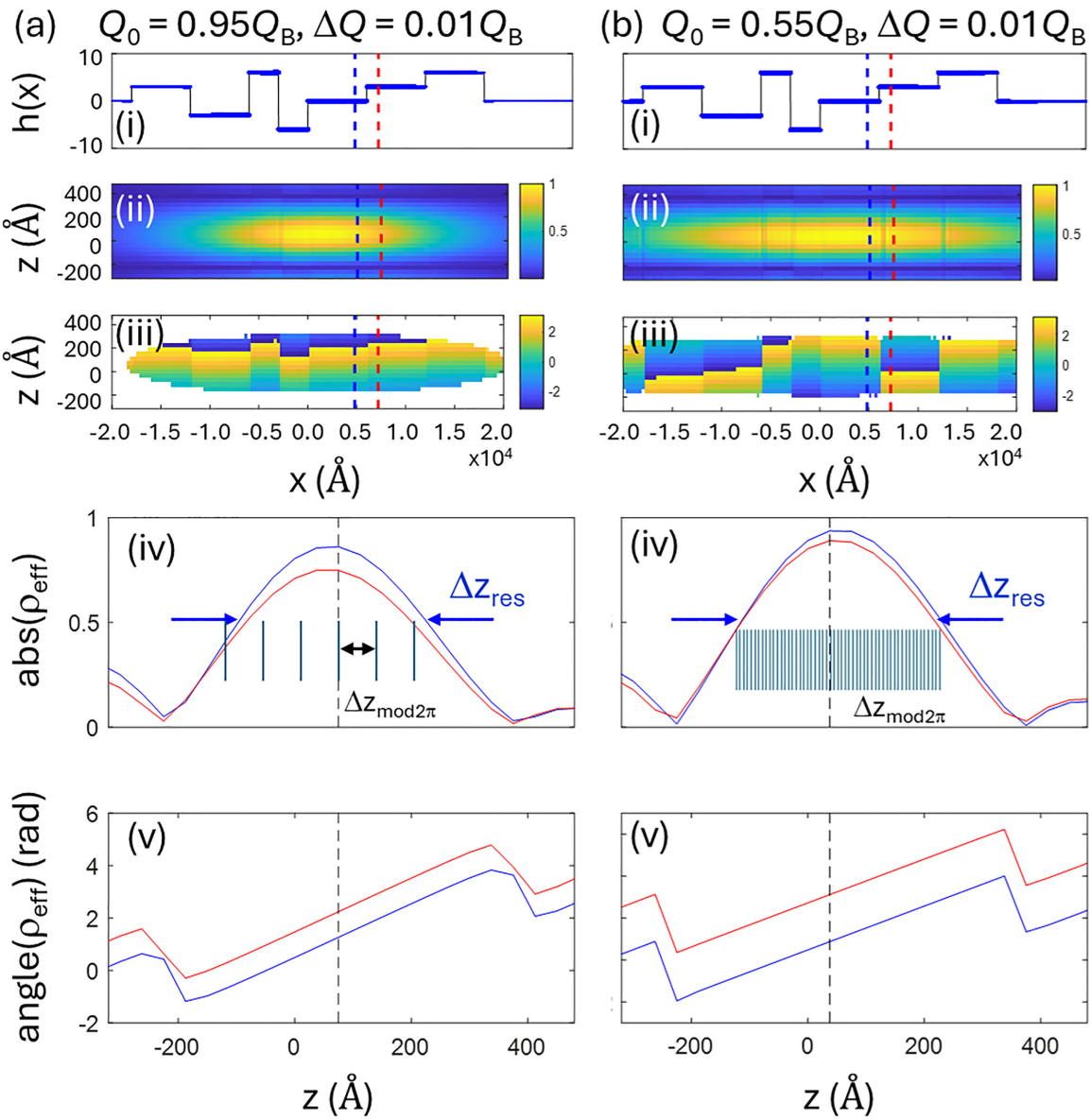

FIG. 6. (i) Original one-dimensional surface topography, *h(x)*, along with the vertical Fourier interpolation of the effective densities from Figs. 5(i) and 5(ii), for two scattering conditions: (a) $Q_z^0 = 0.95\,Q_B$ and (b) $Q_z^0 = 0.55\,Q_B$, both using a ROI of size $\Delta Q_z = \Delta Q_x = 0.01Q_B$. For each case the (ii) amplitude and (iii) phase of the interpolated effective densities are shown. Vertical line scans at the locations of the red and blue dashed lines (corresponding to terraces that differ in height by one unit cell) are shown for the (iv) amplitude and (v) phase. While the difference in surface height (of $c_s = 3$ Å) at these two locations is not observable in the amplitude images [(ii)] and plots [(iv)], distinct phase shifts are observed in the phase images [(iii)] and plots [(v)]. Also shown in (iv) are the different solutions that differ in height by the modulo-2π ambiguity discussed in the text.

$0.01Q_B$. The recovered topography reproduces the original topography for $Q_z^0 = 0.95\,Q_B$. In that example, the modulo-2π ambiguity of height is $\Delta z_{mod2\pi} = \frac{c_s}{0.05} = 20c_s = 60$ Å, is smaller than (but comparable to) the vertical resolution, $\Delta z_{res} \sim \frac{c_s}{0.01} = 100c = 300$ Å. That is, there are ~ 5 different surface heights within the envelope defined by the vertical resolution that are nominally consistent with the observed phase [vertical dashed lines, Fig. 6(a-iv)]. That the original topography was reproduced suggests that the criterion in Eq. (16) may be stricter than necessary. In comparison, the effective density obtained at $Q_z^0 = 0.55\,Q_B$ has a modulo-2π height ambiguity, $\Delta z_{\text{mod-}2\pi} = \frac{c_s}{0.45} = 2.2c_s \sim 6.3$ Å, with the same resolution of ~ 300 Å, leading to 47 different surface heights consistent with height determined from the effective density amplitude [vertical lines, Fig. 6(b-iv)]. Recalling that differences in the original and recovered topographies at $Q_z^0 = 0.55\,Q_B$ were observed to differ by multiples of ± 6.3 Å, and that the recovered step heights had values that were not multiples of the vertical lattice spacing, c_s, we conclude that the deviations between the recovered and actual topography are due to the modulo-2π height ambiguity. We note that knowledge of the actual elementary step height (derived from the crystal structure) could be used to recover the actual topography by selecting the modulo-2π height offsets for each terrace that allows all step heights to be multiple of the vertical lattice spacing, c_s.

A second criterion concerning robust interfacial imaging by CXR is to maximize the sensitivity of the data to the topography itself so that the imaged effective density is robust to any "noise" associated with actual data and any instabilities that may result from the phase recovery process. The derived functional form for the effective density $\exp[iQ_z^0 h(x,y)c_s]$ [Eq. (8)] shows that the sensitivity to topography increases away from the Bragg peak, proportional to $(Q_z^0 - Q_B)$. At the same time, the available signal decreases away from the Bragg peak, proportional to $1/(Q_z^0 - Q_B)^2$, due to the CTR shape. Consequently, the optimal scattering condition to maximize the combination of sensitivity, uniqueness, signal while uniquely recovering the surface topography will be adjacent to a Bragg peak. Conversely, if the desired information is the lateral location of steps (rather than the actual terrace heights), then the optimal measurement will be closer to the anti-Bragg position, which is the point on the CTR that is furthest from the Bragg peak while maintaining sufficient scattering intensities.

E. Limitations and extensions of the current formalism

The derived formalism incorporates an implicit assumption which is that the intensities in the 3D reciprocal space volume could be calculated using a fixed setting of the sample (e.g., at a single incident angle and beam footprint). There are, however, multiple factors that can change the beam footprint during a rocking scan measurement. We discuss two of them: The first factor is the change in beam footprint size during the rocking scan due to changes in the incident angle that is needed to sweep out a volume in reciprocal space within the scattering plane. A second is a change in the position of the beam footprint that would arise due to misalignments of the sample with respect to the rotation center.

First, to evaluate the effect of changes in beam footprint size, we use the conditions chosen for the simulations in Figs. 5 and 6. That is, an incident beam of FWHM = 0.5 μm and energy of $E = 10$ keV; a substrate of layer spacing of $c_s = 3$ Å; a ROI located at $Q_z^0 = 0.95\,Q_B = 1.99$ Å^{-1}, and of size of $\Delta Q_z = \Delta Q_x = 0.01 Q_B = 0.021$ Å^{-1}, corresponding to a resolution of 30 nm. At these conditions, the incident angle is 11.3°, corresponding to a beam footprint of 2.55 μm, and this will change by 5% across the full angular rocking scan range (0.6°) corresponding to the lateral ROI size. We therefore expect that the imaged densities will not be strongly influenced by these small changes at the edges of the illuminated region since the effective densities, as presented here, are analyzed only for regions where the illumination exceeds a threshold of 10% with respect to the maximum illumination. A second consideration for this measurement is that the angular step size in the rocking curve scan (i.e., within the scattering plane) needs to be $\leqslant 0.002°$ to have an oversampling ratio of $\geqslant 3.6$ along the beam footprint, and this requires 300 images to be taken within the 0.6° rocking scan range. At the same time an oversampling factor of 9 for the transverse footprint size is easily achieved by typical experimental conditions (i.e., a detector pixel size of 55 μm, at a detector distance of 2 m). This reveals that the limiting factor in these measurements will be the number of images (and time) needed to oversample the beam footprint within the scattering plane. In comparison, for a measurement at $Q_z^0 = 0.55\,Q_B = 1.99$ Å^{-1}, we can expect a 15% change in the beam footprint during the rocking scan for the same ROI window size, and the total number of measurements would need to increase to 500 to maintain the same oversampling ratio.

Second, we investigate the effect of sample misalignment. Any sample misalignment with respect to the rotation center of the diffractometer would cause the incident beam footprint to translate across the surface during the rocking scan, changing the illuminated region. If we apply the same criterion to the experimental conditions described above (i.e., requiring that any shift of the beam position to be < 5% of the beam footprint), we estimate that the misalignment of the sample height would need to be < 1.2 μm. Since this is substantially larger than the assumed beam size (0.5 μm), a suitable alignment of the sample can be achieved by a traditional lineup procedure.

The specific impact of these factors will need to be understood by systematically incorporating these behaviors into simulations of the measured intensities. One possible extension of this work would be to use the ideas of ptychographic imaging [28] to use the changes in sample illumination to increase the stability of the phase recovery process and remove the implicit limitation on resolution imposed by these systematic errors. This would be especially useful for CXR measurements that require a larger range of incident angles: either to achieve higher lateral resolution within the scattering plane for measurements in the CTR regime; or for measurements at smaller incident angles (especially closer to the total external reflection condition, $\theta \sim 1°$) where the range of incident angles needed to achieve a given resolution is larger due to the smaller vertical momentum transfer.

IV. CONCLUSIONS

A theoretical formalism was developed for coherent specular reflectivity from topographically rough surfaces of semi-infinite crystalline solids. The formalism shows that the interface is imaged as a complex-valued effective density. It has a vertical width defined by the vertical resolution, $2\pi/\Delta Q_z$, that follows the surface topography, and a lateral variation that is controlled primarily by the beam illumination. The phase of the complex-valued effective density has a lateral variation that is controlled by the surface topography $h(x, y)$, and a vertical variation controlled by the measurement conditions (e.g., Q_z^0 and ΔQ_z). This formalism also reveals the important role of coordinate transformations in the interpretation of the observed density due to the nonorthogonal ROI and uses simulations to illustrate some of the key principles to recover surface topography from the complex densities.

Comparison to previous work reveals some important developments. The early work of Vartanyants *et al.* (prior to the revolution in coherent x-ray sources and imaging) recovered interfacial topography by constraining the beam shape [23]. The present results show that the amplitude of the effective density provides an image of the beam illumination (albeit with some artifacts associated with the topography), suggesting that this prior constraint on the analysis may not be necessary (that is, assuming the phase retrieval process for CXR is robust). This approach therefore has the potential

to be used to characterize the beam shape, especially when using well-characterized surfaces. The work of Zhu *et al.* imaged surfaces using a ptychographic approach [28], leading to successful images of phase changes across steps, but not the topography itself. One distinction between those results is that their measurements did not use "rocking curves" to probe a 3D ROI but instead measured the 2D slices of reciprocal space data as a function of beam position. Our analysis shows how 3D reciprocal space data sets can be used to uniquely determine the surface topography from the change in phase between terraces (at least in principle) by distinguishing the vertical and lateral contributions to the phase of the effective interfacial density. An extension of this approach for the case of ptychographic imaging would be beneficial. Finally, we have shown that the topographic sensitivity of the XRIM technique, which is observed using focused incoherent x-ray beams with an objective lens [32,33,45] is analogous to the amplitude probed here by CXR. Also, the XRIM measurements inherently image the interface projected onto the detector plane, while the CXR approach provides a true 3D image of the interface of interest which will be particularly useful for understanding the structure of thin films where the different interfaces can be distinguished (if their vertical separation is resolved by the measurement).

This understanding of CXR highlights important similarities and distinctions with respect to that obtained by BCDI from isolated nanoparticles, most notably for the phase of the recovered density. The phase of the complex density in BCDI reflects the spatial variation of the lattice displacements within a nanoparticle which can be related to lattice strain (i.e., the deviations from perfect crystallinity). The present results show that the lateral variation of the interfacial phase obtained by CXR is defined by the interfacial topography (i.e., deviations from a flat surface). In both cases the magnitude of the lattice displacements in BCDI and topographic variations in CXR are significantly smaller than the spatial resolution of the images (but the respective images of their variation are limited by resolution). An important difference between BCDI and CXR is their interface specificities. Interfacial information (e.g., the particle topography) is seen by BCDI measurements as the termination of the particle density, i.e., as an isosurface defined by a fixed threshold value. Such images are not, however, interface specific as the densities also include contributions from the particle's interior density. In contrast, the CXR formalism that we report here provides a general approach for interface-specific imaging (as illustrated by the absence of any substrate density below the surface in the imaged densities). The distinction between these approaches can be illustrated by noting that, for example, the interface location inferred by BCDI might be sensitive to several extrinsic factors, such as the spatial resolution of the measurement and the chosen threshold value. In contrast, the formalism for CXR provides a direct approach to determine the interfacial topography that is, in principle, independent of the experimental resolution along the surface normal direction. Notably, the observed phase of the effective density provides topographic information (i.e., elementary steps) with substantially higher sensitivity than the vertical resolution of the data ($\sim$10's of nm's). In previous work [34], we also demonstrated how the effective density magnitude of heteroepitaxial interfaces appear equivalent to that of isolated interfaces, except that the observed interfacial density is reduced with respect to an isolated surface corresponding to the change in structure factor across the interface.

This methodology follows the same measurement and phasing process as that used in BCDI measurements (i.e., measurement of a rocking curve corresponding to the sampling of diffracted intensities within a 3D reciprocal space volume followed by its numerical processing using phasing algorithms). Consequently, the present formalism can be used to directly augment the information obtained in a BCDI measurement by creating interface-specific images of selected nanoparticle interfaces through analysis of the associated truncation rods. In other words, this interfacial imaging approach can be thought of as a "dark field" imaging capability, similar to the use of dark field imaging of complex structures by other forms of x-ray imaging [46–49]. Within the context of a BCDI measurement, this approach can use diffuse scattering signals to isolate a particular substructure (e.g., an interface) within complex samples. This will be complementary to the approach in which such features are seen through the recovered strain fields [20]. Another important potential impact of these results is that it should enable the phasing of BCDI data from samples having multiple crystals with different orientations (i.e., mosaic disorder). Such samples are challenging since the BCDI approach is implicitly referenced to a single ideal lattice where the lattice planes have an orientation that is specified by the Bragg peak [50]. Consequently, the phasing of data from crystals that are highly deformed or with distinct orientations is generally extremely challenging as there is no single basis for which to understand the structure of multiple misoriented particles [51]. The present results suggest that the phasing of the truncation rods from two neighboring rotated particles should be straightforward since there is no implicit crystalline basis for the interfacial images as there is in BCDI. Instead, such samples should be equivalent to imaging surfaces of single nanoparticles without opposing facets. We expect that the relative position of those interfaces will be encoded through the interference in their respective scattering intensities. By doing such an analysis for different truncation rods, we expect that the shapes of the different particles (seen by the interfaces) can be reconstructed even when the phasing of BCDI would otherwise be challenging.

ACKNOWLEDGMENTS

This material is supported by the U.S. Department of Energy, Office of Science, Office of Basic Energy Sciences, Geoscience Research Program (FWP 57814) under Contract No. DE-AC02-06CH11357. I.C.-A. would like to acknowledge the European Funding "Next Generation EU" through the program "María Zambrano", a joint effort of the University of Zaragoza and the Spanish University Council. She also acknowledges financial support from the Spanish Agencia Estatal de Investigación, through Project No. PID2020-115159GB-I00/AEI/10.13039/501100011033 and the Aragonese Project No. RASMIA E12-23R cofunded by Fondo Social Europeo of the European Union FEDER (ES).

DATA AVAILABILITY

The data that support the findings of this article are openly available [52], embargo periods may apply.

[1] R. Hettel, DLSR design and plans: An international overview, J. Synchrotron Radiat. **21**, 843 (2014).

[2] M. Borland, G. Decker, L. Emery, V. Sajaev, Y. P. Sun, and A. M. Xiao, Lattice design challenges for fourth-generation storage-ring light sources, J. Synchrotron Radiat. **21**, 912 (2014).

[3] P. Raimondi, C. Benabderrahmane, P. Berkvens, J. C. Biasci, P. Borowiec, J. F. Bouteille, T. Brochard, N. B. Brookes, N. Carmignani, L. R. Carver, J. M. Chaize, J. Chavanne, S. Checchia, Y. Chushkin, F. Cianciosi, M. Di Michiel, R. Dimper, A. D'Elia, D. Einfeld, F. Ewald, *et al.*, The extremely brilliant source storage ring of the european synchrotron radiation facility, Commun. Phys. **6**, 82 (2023).

[4] J. L. Bañuelos, E. Borguet, G. E. Brown, R. T. Cygan, J. J. DeYoreo, P. M. Dove, M. P. Gaigeot, F. M. Geiger, J. M. Gibbs, V. H. Grassian, A. G. Ilgen, Y. S. Jun, N. Kabengi, L. Katz, J. D. Kubicki, J. Lutzenkirchen, C. V. Putnis, R. C. Remsing, K. M. Rosso, G. Rother, *et al.*, Oxide- and silicate-water interfaces and their roles in technology and the environment, Chem. Rev. **123**, 6413 (2023).

[5] B. E. Warren, *X-Ray Diffraction* (Dover, New York, 1990).

[6] A. Guinier, *X-Ray Diffraction In Crystals, Imperfect Crystals, and Amorphous Bodies* (Dover, New York, 1994).

[7] S. K. Sinha, E. B. Sirota, S. Garoff, and H. B. Stanley, X-ray and neutron-scattering from rough surfaces, Phys. Rev. B **38**, 2297 (1988).

[8] J. W. Miao, T. Ishikawa, I. K. Robinson, and M. M. Murnane, Beyond crystallography: Diffractive imaging using coherent x-ray light sources, Science **348**, 530 (2015).

[9] J. R. Fienup, Reconstruction of an object from the modulus of its Fourier transform, Opt. Lett. **3**, 27 (1978).

[10] J. R. Fienup, Phase retrieval algorithms - A comparison, Appl. Opt. **21**, 2758 (1982).

[11] S. Marchesini, A unified evaluation of iterative projection algorithms for phase retrieval, Rev. Sci. Instrum. **78**, 011301 (2007).

[12] M. A. Pfeifer, G. J. Williams, I. A. Vartanyants, R. Harder, and I. K. Robinson, Three-dimensional mapping of a deformation field inside a nanocrystal, Nature (London) **442**, 63 (2006).

[13] J. Miao, J. Kirz, and D. Sayre, The oversampling phasing method, Acta Crystallogr. D **56**, 1312 (2000).

[14] G. J. Williams, M. A. Pfeifer, I. A. Vartanyants, and I. K. Robinson, Internal structure in small Au crystals resolved by three-dimensional inversion of coherent x-ray diffraction, Phys. Rev. B **73**, 094112 (2006).

[15] M. O. Hill, I. Calvo-Almazan, M. Allain, M. V. Holt, A. Ulvestad, J. Treu, G. Koblmuller, C. Huang, X. Huang, H. Yan, E. Nazaretski, Y. S. Chu, G. B. Stephenson, V. Chamard, L. J. Lauhon, and S. O. Hruszkewycz, Measuring three-dimensional strain and structural defects in a single InGaAs nanowire using coherent x-ray multiangle bragg projection ptychography, Nano Lett. **18**, 811 (2018).

[16] I. K. Robinson and R. Harder, Coherent x-ray diffraction imaging of strain at the nanoscale, Nat. Mater. **8**, 291 (2009).

[17] P. Thibault, M. Dierolf, O. Bunk, A. Menzel, and F. Pfeiffer, Probe retrieval in ptychographic coherent diffractive imaging, Ultramicroscopy **109**, 338 (2009).

[18] P. Thibault and V. Elser, X-ray diffraction microscopy, Annu. Rev. Condens. Matter Phys. **1**, 237 (2010).

[19] P. Li, M. Allain, T. A. Grünewald, M. Rommel, A. Campos, D. Carbone, and V. Chamard, 4th generation synchrotron source boosts crystalline imaging at the nanoscale, Light.-Sci. Appl. **11**, 73 (2022).

[20] Y. F. Sun and A. Singer, Bragg coherent diffractive imaging for defects analysis: Principles, applications, and challenges, Chem Phys Rev **5**, 031310 (2024).

[21] I. Calvo-Almazán, V. Chamard, T. A. Grünewald, and M. Allain, Inhomogeneous probes for Bragg coherent diffraction imaging: Toward the imaging of dynamic and distorted crystals, Phys. Rev. B **110**, 134117 (2024).

[22] A. F. Suzana, S. S. Lee, I. Calvo-Almazan, W. Cha, R. Harder, and P. Fenter, Visualizing the internal nanocrystallinity of calcite due to nonclassical crystallization by 3D coherent x-ray diffraction imaging, Adv. Mater. **36**, e2310672 (2024).

[23] I. A. Vartanyants, J. A. Pitney, J. L. Libbert, and I. K. Robinson, Reconstruction of surface morphology from coherent x-ray reflectivity, Phys. Rev. B **55**, 13193 (1997).

[24] I. A. Vartanyants, I. K. Robinson, I. McNulty, C. David, P. Wochner, and T. Tschentscher, Coherent x-ray scattering and lensless imaging at the european XFEL facility, J. Synchrotron Radiat. **14**, 453 (2007).

[25] M. Chu, J. Zhang, M. Wojcik, T. Sun, M. Sprung, and J. Wang, Probing three-dimensional mesosocopic interfacial structures in a single view using multibeam x-ray coherent surface scattering and holography imaging, Nat. Commun. **14**, 5795 (2023).

[26] G. X. Ju, D. W. Xu, M. Highland, C. Thompson, H. Zhou, J. A. Eastman, P. H. Fuoss, P. Zapol, H. Kim, and G. B. Stephenson, Coherent x-ray spectroscopy reveals the persistence of island arrangements during layer-by-layer growth, Nat. Phys. **15**, 589 (2019).

[27] R. L. Headrick, J. G. Ulbrandt, P. Myint, J. Wan, Y. Li, A. Fluerasu, Y. Zhang, L. Wiegart, and K. F. Ludwig Jr., Coherent X-ray measurement of step-flow propagation during growth on polycrystalline thin film surfaces, Nat. Commun. **10**, 2638 (2019).

[28] C. H. Zhu, R. Harder, A. Diaz, V. Komanicky, A. Barbour, R. Q. Xu, X. J. Huang, Y. H. Liu, M. S. Pierce, A. Menzel, and H. You, Ptychographic x-ray imaging of surfaces on crystal truncation rod, Appl. Phys. Lett. **106**, 101604 (2015).

[29] J. Als-Nielsen and D. McMorrow, *Elements of Modern X-ray Physics* (Wiley, Chichester, 2001).

[30] I. K. Robinson, Crystal truncation rods and surface-roughness, Phys. Rev. B **33**, 3830 (1986).

[31] M. S. Pierce, V. Komanicky, A. Barbour, D. C. Hennessy, J. D. Suc, A. Sandy, C. Zhu, and H. You, *In situ* coherent x-ray scattering and scanning tunneling microscopy studies of

hexagonally reconstructed Au(001) in electrolytes, ECS Trans. **35**, 71 (2011).

[32] P. Fenter, C. Park, Z. Zhang, and S. Wang, Observation of subnanometre-high surface topography with x-ray reflection phase-contrast microscopy, Nat. Phys. **2**, 700 (2006).

[33] P. Fenter, C. Park, V. Kohli, and Z. Zhang, Image contrast in x-ray reflection interface microscopy: Comparison of data with model calculations and simulations, J. Synchrotron Radiat. **15**, 558 (2008).

[34] P. Fenter and I. Calvo-Almazán, Imaging interfacial topography with coherent x-ray reflectivity, Phys. Rev. B **109**, 094112 (2024).

[35] I. A. Vartanyants and I. K. Robinson, Partial coherence effects on the imaging of small crystals using coherent x-ray diffraction, J. Phys.: Condens. Matter **13**, 10593 (2001).

[36] K. A. Nugent, A. G. Peele, H. M. Quiney, and H. N. Chapman, Diffraction with wavefront curvature: A path to unique phase recovery, Acta Crystallogr. A **61**, 373 (2005).

[37] W. Rudin, *Real and Complex Analysis* (McGraw-Hill, New York, 1987).

[38] P. Fenter, X-ray reflectivity as a probe of mineral-fluid interfaces: A user guide, Rev. Mineral. Geochem. **49**, 149 (2002).

[39] See Supplemental Material at http://link.aps.org/supplemental/10.1103/q75z-gk3l for an illustration showing that the intrinsic effective density $\rho_{\text{eff-0}}$ (shown in Fig. 2) is independent of the beam attenuation β. It also shows a detailed derivation of Eq. (11), which also includes Refs. [37,40,41].

[40] P. Li, S. Maddali, A. Pateras, I. Calvo-Almazan, S. O. Hruszkewycz, W. Cha, V. Chamard, and M. Allain, General approaches for shear-correcting coordinate transformations in Bragg coherent diffraction imaging. Part II, J. Appl. Crystallogr. **53**, 404 (2020).

[41] S. Maddali, P. Li, A. Pateras, D. Timbie, N. Delegan, A. L. Crook, H. Lee, I. Calvo-Almazan, D. Sheyfer, W. Cha, F. J. Heremans, D. D. Awschalom, V. Chamard, M. Allain, and S. O. Hruszkewycz, General approaches for shear-correcting coordinate transformations in Bragg coherent diffraction imaging. Part I, J. Appl. Crystallogr. **53**, 393 (2020).

[42] M. J. Bedzyk and P. Fenter, in *The X-ray Standing Wave Technique: Principles and Applications*, edited by J. Zegenhagen, and A. Kazimirov (World Scientific, Singapore, 2013), p. 289.

[43] L. Cheng, P. Fenter, M. J. Bedzyk, and N. C. Sturchio, Fourier-expansion solution of atom distributions in a crystal using x-ray standing waves, Phys. Rev. Lett. **90**, 255503 (2003).

[44] Z. Zhang, P. Fenter, L. Cheng, N. C. Sturchio, M. J. Bedzyk, M. L. Machesky, and D. J. Wesolowski, Model-independent x-ray imaging of adsorbed cations at the crystal-water interface, Surf. Sci. **554**, L95 (2004).

[45] N. Laanait, E. B. R. Callagon, Z. Zhang, N. C. Sturchio, S. S. Lee, and P. Fenter, X-ray-driven reaction front dynamics at calcite-water interfaces, Science **349**, 1330 (2015).

[46] F. Pfeiffer, M. Bech, O. Bunk, P. Kraft, E. F. Eikenberry, C. Brönnimann, C. Grünzweig, and C. David, Hard-x-ray dark-field imaging using a grating interferometer, Nat. Mater. **7**, 134 (2008).

[47] M. C. Zdora, State of the art of x-ray speckle-based phase-contrast and dark-field imaging, J. Imaging **4**, 60 (2018).

[48] M. Bech, O. Bunk, T. Donath, R. Feidenhans'l, C. David, and F. Pfeiffer, Quantitative x-ray dark-field computed tomography, Phys. Med. Biol. **55**, 5529 (2010).

[49] H. Simons, A. King, W. Ludwig, C. Detlefs, W. Pantleon, S. Schmidt, I. Snigireva, A. Snigirev, and H. F. Poulsen, Dark-field X-ray microscopy for multiscale structural characterization, Nat. Commun. **6**, 6098 (2015).

[50] G. J. Williams, M. A. Pfeifer, I. A. Vartanyants, and I. K. Robinson, Three-dimensional imaging of microstructure in Au nanocrystals, Phys. Rev. Lett. **90**, 175501 (2003).

[51] X. W. Shi, J. N. Clark, G. Xiong, X. J. Huang, R. Harder, and I. K. Robinson, Mechanical breakdown of bent silicon nanowires imaged by coherent x-ray diffraction, New J. Phys. **15**, 123007 (2013).

[52] Original data shown in Figs. 1, 2, 4, 5, and 6 are archived at https://doi.org/10.18126/t0ca-5645.